Top–down estimates of black carbon emissions at high latitudes using an atmospheric transport model and a Bayesian inversion framework

Nikolaos Evangeliou *, Rona L. Thompson, Sabine Eckhardt, Andreas Stohl

Norwegian Institute for Air Research (NILU), Department of Atmospheric and Climate Research (ATMOS), Kjeller, Norway.

* Correspondence to: N. Evangeliou (nikolaos.evangeliou@nilu.no)

12 **Abstract**

13   This paper presents the results of BC inversions at high northern latitudes (>50°N) for

14 the 2013–2015 period. A sensitivity analysis was performed to select the best representative

15 species for BC and the best a priori emission dataset. The same model ensemble was used to

16 assess the uncertainty of the a posteriori emissions of BC due to scavenging and removal and

17 due to the use of different a priori emission inventory. A posteriori concentrations of BC

18 simulated over Arctic regions were compared with independent observations from flight and

19 ship campaigns showing, in all cases, smaller bias, which in turn witnesses the success of the

20 inversion. The annual a posteriori emissions of BC at latitudes above 50°N were estimated as

21 560 ± 171 kt yr^{-1}, significantly smaller than in ECLIPSEv5 (745 kt yr^{-1}), which was used and

22 the a priori information in the inversions of BC. The average relative uncertainty of the

23 inversions was estimated to be 30%.

24   A posteriori emissions of BC in North America are driven by anthropogenic sources,

25 while biomass burning appeared to be less significant as it is also confirmed by satellite

26 products. In North Europe, a posteriori emissions were estimated to be half compared to the a

27 priori ones, with the highest releases to be in megacities and due to biomass burning in

28 Eastern Europe. The largest emissions of BC in Siberia were calculated along the transect

29 between Yekaterinsburg and Chelyabinsk. The optimised emissions of BC were high close to

30 the gas flaring regions in Russia and in Western Canada (Alberta), where numerous power

31 and oil/gas production industries operate. Flaring emissions in Nenets-Komi oblast (Russia)

32 were estimated to be much lower than in the a priori emissions, while in Khanty-Mansiysk

33 (Russia) they remained the same after the inversions of BC. Increased emissions in the

34 borders between Russia and Mongolia are probably due to biomass burning in villages along

35 the Trans-Siberian Railway. The maximum BC emissions in high northern latitudes (>50°N)

36 were calculated for summer months due to biomass burning and they are controlled by

37 seasonal variations in Europe and Asia, while North America showed a much smaller

38 variability.

1 Introduction

Light absorbing species, such as black carbon (BC), are the main components of atmospheric particulate matter, affecting air quality, weather and climate. BC originates from the incomplete combustion of fossil fuels (primarily coal and diesel), from open high–temperature combustion of natural gas in the oil/gas field (gas flaring), as well as from the burning of biomass and biofuels. BC particles affect cloud formation and precipitation as they act as cloud condensation nuclei in their hydrophilic form (Wang et al., 2016). BC is also a major driver of climate change contributing to global warming with a radiative forcing at the top of the atmosphere ranging between 0.17 and 0.71 W m^{-2} (Bond et al., 2013; Myhre et al., 2013; Wang et al., 2014). BC deposited in Arctic snow surfaces in concentrations of up to 30 ng g^{-1} can reduce snow albedo by 1–3% (Hegg et al., 2009) in fresh snow and up to 3 times more as snow ages and the BC particles become more concentrated (Clarke and Noone, 1985). Airborne BC also warms the air and reduces tropical cloudiness by absorbing the incoming solar radiation (Ackerman, 2000). It also reduces atmospheric visibility and increases aerosol optical depth (Jinhuan and Liquan, 2000). From a health perspective, BC particles, generally being sub-micron in size, can penetrate into the lungs and cause pulmonary diseases (e.g., Wang et al., 2014).

To improve understanding about how BC affects climate and to develop effective policies to tackle BC's associated environmental problems requires accurate knowledge of the emissions and their spatiotemporal distribution. Most commonly, BC emission inventory datasets are built by "bottom up" approaches, which are based on activity data and emission factors and proxy information for spatial disaggregation, but these methods are considered to have large uncertainties (Cao et al., 2006). Numerous global or regional emission inventories of BC have been constructed previously (Bond et al., 2004; Schaap et al., 2004; Streets et al., 2003); nevertheless, emission uncertainties contribute significantly to the overall uncertainty of modelled concentrations of BC. Emission uncertainties affect even more significantly regional/episodic simulations, as in many cases emissions deviate from the annual mean. Such studies represent a useful tool to improve our understanding of the relationship between observed concentrations of BC and BC emissions. Furthermore, BC emissions have their most pronounced effect on the regional scale due to the relatively short atmospheric lifetime of BC (Hodnebrog et al., 2014; Samset et al., 2014),.

The relative differences between different emission inventories are largest for the high latitudes (AMAP, 2015) and particularly in high-latitude Russia where emission information is poor. For this area, a new satellite-based high-resolution inventory showed that BC

74 emissions from Biomass Burning (BB) might have been 3.5 times higher than emissions
75 given in the Global Fire Emissions Database (GFEDv4) (Hao et al., 2016), if more realistic
76 emission factors are used (May et al., 2014). Furthermore, new sources of BC in the same
77 area have been identified recently. For example, emissions from gas flaring by the oil industry
78 have been missing from most emission inventories and may be an important source of BC at
79 high latitudes (Stohl et al., 2013). For instance, in 2008 Russia was responsible for nearly one
80 third of the gas flared globally (Elvidge et al., 2009). However, the gas flaring source is
81 highly uncertain. For example, based on isotopic measurements, Winiger et al. (2017)
82 reported recently that the contribution from gas flaring to BC measured at Tiksi in Siberia is
83 lower than estimated by Stohl et al. (2013), while recently published bottom-up inventories
84 (Huang et al., 2015; Huang and Fu, 2016) suggested even higher gas flaring emissions.
85 Finally, Popovicheva et al. (2017) reported that one existing emission dataset of BC captured
86 surface concentrations in the Russian Arctic quite efficiently.

87   In this study, we estimated the BC emissions at high northern latitudes using
88 atmospheric observations of BC in a Bayesian inversion framework. Emissions were
89 estimated for the region north of 50°N because this is the region with the largest influence on
90 Arctic surface concentrations (Klonecki, 2003; Stohl, 2006). We determine the emissions
91 with monthly time resolution for the years 2013, 2014 and 2015. We first describe the
92 observation data, the transport model and the Bayesian inversion technique used, as well as
93 the prior emission information. We then assess the sensitivity of the transport model to
94 different scavenging coefficients (below-cloud and in-cloud) for BC and to different emission
95 inventories. We finally present optimised BC emissions, discuss these results in comparison
96 with independent estimates and calculate the uncertainty of the inversions with respect to
97 different scavenging parameters used for BC and using four different prior emission datasets.

2 Methodology

2.1 Observation network

100   Atmospheric observations of BC were retrieved from the World Data Centre for
101 Aerosols (http://ebas.nilu.no) and from the International Arctic Systems For Observing The
102 Atmosphere (http://www.esrl.noaa.gov/psd/iasoa/). An overview of the stations used in this
103 paper can be found in Table 1 and Figure 1a–c. The selected measurements were performed
104 with different types of instruments that may differ substantially. When measurements are

based on light absorption we refer to Equivalent BC (EBC), while measurements based on thermal-optical methods refer to elemental carbon (EC) (Petzold et al., 2013).

At Alert (ALT), Appalachian (APP), Asprveten (ASP), Birkenes (BIR), East Trout Lake (ETL), South Great Planes (SGP), Steamboat Springs (COL), Trinidad Head (TRI) and Whistler (WHI) measurements were performed with particle soot absorption photometers (PSAPs). At Annaberg-Buchholz (ANB), Bösel (BOS), Cabauw Zijdeweg (CAB), Hyytiälä (HYY), Leipzig (LEI), Melpitz (MEL), Nepal Climate Observatory (NEP), Pallas (PAL), Ústí n.L.-mesto (ULM) and Waldhof (WLD) the particle light absorption coefficient was measured by multi-angle absorption photometers (MAAP; Petzold and Schönlinner, 2004), which are in excellent agreement with other particle light absorption photometers such as a photoacoustic sensor (e.g., Muller et al., 2011). In the MAAP instrument, particles are continuously sampled on filter tape, with loaded spots subsequently analysed by Raman spectroscopy to derive the particle mass concentration of soot (Nordmann et al., 2013). The cut-off sizes of the different MAAP instruments varied between 1 and 10 μm. Continuous light absorption photometers (CLAP, Model PSAP; 565 nm) were used at Barrow (BAR), Bondville (BON), Gosan (GOS), K-puszta (KPU), BEO Moussala (MOU) and Summit (SUM). Although these instruments were calibrated to measure the aerosol absorption coefficient, a previous study at this site revealed that a value of 10 m^2 g^{-1} is a reasonable conversion factor to determine the BC concentration (Gelencsér et al., 2000). Aethalometers were used at Tiksi (TIK) and Zeppelin (ZEP).

All these stations measure the particle light absorption coefficients of different size fractions of the aerosol at wavelengths around 530–550 nm. Then the light absorption coefficients are converted to EBC mass concentrations under certain assumptions (Petzold et al., 2013). This is done externally for instruments such as MAAP, CLAP, PSAP etc. using a mass absorption efficiency of 10 m^2 g^{-1} (Bond and Bergstrom, 2006). For aethalometers, the conversion is done internally by the instrument. All station measurements are routinely filtered to remove influence from local sources.

2.2 Source – Receptor Relationships (SRRs)

We used the Lagrangian Particle Dispersion Model (LPDM), FLEXible PARTicle dispersion model (FLEXPART) (Stohl et al., 1998, 2005) to model atmospheric transport. Using LPDMs to model particle or trace gas concentrations has several advantages over Eulerian models, namely they can have quasi-infinite resolution and they are not subject to numerical diffusion. Thus they can provide better resolved source-receptor relationship (SRR)

fields, which describe the relationship between the sensitivity of a "receptor" to a "source" element, as described by Seibert and Frank (2004). SRRs for the lowest model level are often called footprint emission sensitivities or even just footprints.

SRRs were calculated using FLEXPART version 10 in a backwards mode (see Stohl et al., 2005) in which computational particles are released backward in time from the observation sites (receptors). When the number of observation sites is smaller than the number of unknown flux grid cells this mode is computationally more efficient than forward calculations. Furthermore, backward simulations can be initiated exactly at the measurement point without initial diffusion of information into a grid cell. This important advantage of LPDMs also facilitates high spatial resolution of the model output around the measurement sites. As meteorological input data, European Centre for Medium-Range Weather Forecasts operational meteorological analyses were used with 137 vertical levels and a horizontal resolution of $0.5°×0.5°$. Retroplumes were calculated at hourly intervals at each of the receptors. 40,000 particles for each retroplume were released and followed 30 days backwards in time. This should be a sufficiently long time in order to include almost all contributions to BC concentration at the receptor given the atmospheric lifetime of BC (in the range of 2–10 days, Benkovitz et al., 2004; Koch and Hansen, 2005; Park et al., 2005; Textor et al., 2006).

The treatment of scavenging is a major uncertainty for modelling BC (Browse et al., 2012). Therefore, an ensemble of 12 model simulations was performed each with different BC tracers having different in–cloud and below–cloud scavenging properties (Table 2). This method allows the sensitivity of the SRRs (produced by FLEXPART) to scavenging to be quantified. Table 2 shows the different below–cloud and in–cloud scavenging parameters used within the model in the sensitivity runs. For all tracers, we assumed a logarithmic size distribution with an aerodynamic mean diameter of 0.25 μm, a logarithmic standard deviation of 0.3 and a particle density of 1500 kg m^{-3} (Long et al., 2013). The dry deposition scheme in FLEXPART is based on the resistance analogy (Slinn 1982). The present version of the model uses the precipitation rate from ECMWF to determine below-cloud scavenging and the cloud liquid water and ice content, precipitation rate and cloud depth from ECMWF to calculate in-cloud scavenging (see Grythe et al., 2017).

The SRR at the lowest model layer (in seconds) (Figure 1g–i) can be multiplied with gridded emission fluxes from a BC emission inventory (in kg m^{-2} s^{-1}) distributed over the layer depth (100 m). This gives the prior concentration of BC at the receptor point (in ng m^{-3}).

2.3 Bayesian inversion

The inversion methodology used in the present study, FLEXINVERT, is described fully in Thompson and Stohl (2014) and has been already used in studies of CH_4, HFC-125, HFC-134a and SF_6 (Brunner et al., 2017; Thompson et al., 2015, 2017). Since atmospheric transport and deposition are linear operations, they can be described as a Jacobian matrix of SRRs (**H**). The BC concentrations (y) can then be modelled given an estimate of the emissions (x) as follows:

$$y = \mathbf{H}(x) + \varepsilon \qquad (1)$$

where ε is an error associated with model representation, such as the modelled transport and deposition as well as the measurements. Since **H** is generally not invertible (or may have no unique inverse), statistical optimization methods are used, which require prior information for regularization. According to Bayesian statistics, the problem can be expressed as the maximization of the probability density function of the emissions given the prior information and observations and is equivalent to finding the minimum of the cost function:

$$J(x) = \frac{1}{2}(x - x_b)^T \mathbf{B}^{-1}(x - x_b) + \frac{1}{2}(y - \mathbf{H}x)^T \mathbf{R}^{-1}(y - \mathbf{H}x) \qquad (2)$$

where **B** and **R** are the error covariance matrices for the prior emissions and the observations, respectively. The error in the observation space also accounts for model representation errors that are not related to the BC emissions. The emissions that minimize the cost function can be found by solving the first order derivative of equation (2). Hence, the following equation can be derived for the most probable emissions, x (for details see e.g. Tarantola, 2005):

$$x = x_b + \mathbf{B}\mathbf{H}^T(\mathbf{H}\mathbf{B}\mathbf{H}^T + \mathbf{R})^{-1}(y - \mathbf{H}x_b) \qquad (3)$$

In this study, the state vector contains the monthly unknown surface emissions on the grid of variable resolution (Figure 1d–f) and has a resolution of between $1.0° \times 1.0°$ and $8.0° \times 8.0°$. The total number of emission variables to be determined was 1422 for 2013, 1404 for 2014 and 1436 for 2015. The posterior error covariance matrix, **A**, is equivalent to the inverse of the second derivative of the cost function. However, to account for the uncertainty in the scavenging parameters and different prior information, we instead conduct ensemble of inversions to estimate the posterior uncertainty in order to account for the systematic errors. To do this, we conduct the inversion for BC represented by 12 different scavenging coefficients (see Table 2) and for four different prior emission datasets, and do this for each of the three years of our study (2013–2015). The resulting model ensemble ($12 \times 4 = 48$) for each year defines the posterior uncertainty due to scavenging and use of different a priori information (section 3.3).

203   Since negative values for the posterior emissions are mathematically possible but
204   physically unlikely, we applied a subsequent inequality constraint on the emissions following
205   the method of Thacker (2007). This is a truncated Gaussian approach in which inequality
206   constraints are applied as error-free "observations":

207    $$\hat{x} = x + \mathbf{A}\mathbf{P}^{\mathbf{T}}(\mathbf{P}\mathbf{A}\mathbf{P}^{\mathbf{T}})^{-1}(c - \mathbf{P}x) \qquad (4)$$

208   where **A** is the posterior error covariance matrix, **P** is a matrix operator to select the variables
209   that violate the inequality constraint, and c is a vector of the inequality constraint, which in
210   this case is zero.

211   The emissions were solved on an irregular grid, which has been optimized based on the
212   SRRs to give higher resolution (1.0° × 1.0°) in regions where there is strong contribution
213   from emission sources to BC concentrations and lower (8.0° × 8.0°) where there is a weak
214   contribution (Stohl et al., 2009). Then, the results are interpolated onto a uniform grid of
215   1.0°×1.0° resolution from 180°W to 180°E and 50°N to 90°N and are given at monthly time
216   resolution for 2013, 2014 and 2015. To constrain emissions of BC monthly, a temporal
217   correlation scale length between flux time-steps equal to 90 days was set.

218   **2.4   A priori emission information**

219   In the present study, the emission inventories ECLIPSE (Evaluating the CLimate and
220   Air Quality ImPacts of ShortlivEd Pollutants) version 5 (Klimont et al., 2017) (available here:
221   http://www.iiasa.ac.at/web/home/research/researchPrograms/air/Global_emissions.html),
222   EDGAR (Emissions Database for Global Atmospheric Research) version HTAP_V2.2
223   (Janssens-Maenhout   et   al.,   2015)   (available   here:
224   http://edgar.jrc.ec.europa.eu/methodology.php#), ACCMIP (Emissions for Atmospheric
225   Chemistry and Climate Model Intercomparison Project) version 5 (Lamarque et al., 2013)
226   (available   here: http://accent.aero.jussieu.fr/ACCMIP_metadata.php)   and   MACCity
227   (Monitoring Atmospheric Composition & Climate / megaCITY - Zoom for the ENvironment)
228   (Wang et al., 2014) (available here: http://accent.aero.jussieu.fr/MACC_metadata.php) were
229   used as the prior emission estimates of BC (see Figure 2).

230   The ECLIPSE emission inventory (Figure 2a) accounts for waste burning, industrial
231   combustion and processing, surface transportation that also includes power plants, energy
232   conversion and extraction that also includes gas flaring, residential and commercial
233   combustion.

234   The HTAP_V2 dataset (Figure 2b) consists of high-resolution gridded emissions of BC
235   based on nationally reported emissions combined with regional scientific inventories. It

includes the sources of aviation, inland waterways and marine shipping, energy production other than electricity generation, industrial processes, solvent production and application, electricity generation, ground transport, buildings heating, cooling, equipment, and waste disposal or incineration.

The ACCMIP simulations use the BC emission inventory covering the historical period (1850–2000) provided by (Lamarque et al., 2010), which is built for the climate model simulations in CMIP5 (Figure 2c). Anthropogenic emissions are mainly based on Bond et al. (2004) but apply new emission factors. The year 2000 dataset was used for harmonization with the future emissions determined by Integrated Assessment Models (IAMs) for the four Representative Concentration Pathways (RCP4.5, RCP6, and RCP8.5). They include emissions from energy production and distribution, industry (combustion and non-combustion), transportation, maritime transport and aviation, residential and commercial combustion and solvent extraction, agricultural production and waste treatment.

MACCity (Figure 2d) was built as an extension of the historical emissions dataset of ACCMIP. It provides monthly averaged sectorial emissions for each year during the 1960-2010 period. This dataset was based on the decadal ACCMIP emissions for 1960-2000 and the 2005 and 2010 emissions provided by RCP 8.5. This scenario was chosen since it included some information on recent emissions at the regional scale in Europe and North America. The emission sectors are consistent with Lamarque et al. (2010).

Emissions from biomass burning were adopted from the Global Fire Emissions Database, Version 4 (GFEDv4) (Giglio et al., 2013) and implemented to each of the four emission inventories for 2013, 2014 and 2015. Emissions from gas flaring are only included in ECLIPSEv5 inventory.

3 Results

3.1 Sensitivity to scavenging and selection of the best representative species for BC

The comparison of the simulated and observed concentrations for the 12 different BC tracers (see Table 2) is shown in Taylor diagrams in Figure 3 for ECLIPSEv5 and in Figure S 1 for ACCMIPv5, EDGAR_HTAPv2.2 and MACCity, only for those stations that had continuous measurements for all the years of our study (2013–2015) namely ZEP, SUM, TIK, BAR, PAL, CAB, MEL and LEI (see Table 1). For all the different BC species,

concentrations of BC were calculated using the FLEXPART SRR and the four different emission datasets for 2013, 2014 and 2015.

Correlations of modelled and observed surface concentrations of BC were high (>0.5) only at stations ALT, MEL and LEI that present low normalised standard deviation (NSD) values (<1) and low normalised root mean square error (nRMSE) values. All NSD values were below 1.5 except at TIK and ULM stations (see Figure 3 and Figure S 1). In general, dispersion models fail to reproduce BC concentrations close to TIK station (Eckhardt et al., 2015; Evangeliou et al., 2016), as the station has been reported to receive pollution from local anthropogenic sources (Asmi et al., 2016). ULM station is located on the border between Germany and the Czech Republic and was shown previously to be strongly affected by BC emissions from residential combustion sources (Schladitz et al., 2015). The model-observation mismatches ($[model - observations]/observations$) due to the use of 12 different species for BC can be seen in Figure S 2 for the years 2013, 2014 and 2015. These values are average concentrations from the use of the four different emissions inventories (ECLIPSEv5, ACCMIPv5, EDGAR_HTAPv2.2 and MACCity). The extreme perturbation of the scavenging coefficients of BC caused an average relative model-observation mismatch (normalised against observations) of about 39% in 2013 (Figure S 2) at all stations.

Similar to 2013, 12 species with different scavenging parameters were used for BC following Table 2 in 2014 and the comparison with observations is shown in Taylor diagrams in Figure 3 using ECLIPSEv5 emissions and in Figure S 1 using ACCMIPv5, EDGAR_HTAPv2.2 and MACCity for the common stations. The comparison of surface simulated concentrations with observations showed NSD values above one, high nRMSE values and correlation coefficients below 0.5 in at most of the stations. The main difference from year 2013 is that the model-observation mismatches for the surface concentrations of the 12 BC species was estimated to be 32% in 2014 (Figure S 2), in contrast to 39% in 2013. The same deficiency of the model to capture the spring and summer concentrations of BC was observed. The calculated mismatches were very low in at most of the lower latitude stations and increased towards the remote Arctic ones (Figure S 2).

Finally, in 2015 the comparison of surface concentrations for each of the 12 different BC species using the four different datasets (ECLIPSEv5, ACCMIPv5, EDGAR_HTAPv2.2 and MACCity) with observations showed again the same pattern as in the previous years with most of the NSD values to be above unity, high nRMSE values and low Pearson coefficients (Figure 3 and Figure S 1). The model-observation mismatches of BC concentrations (Figure S 2) were estimated as high as 43% for the stations where full measurements existed for the

three years of the study (2013–2015). Like in the previous years, the model failed to reproduce surface concentrations of BC at some of the remote stations of the Arctic.

We used the NMSE (Normalised Mean Square Error) to select the most representative BC tracer species. The NMSE is an estimator of the overall deviations between predicted and measured values. It is defined as:

$$NMSE = \frac{1}{N}\sum_i \frac{(O_i - P_i)^2}{\overline{P_i}\,\overline{O_i}} \qquad (5)$$

where O_i and P_i are observed and predicted concentrations, N the number of observations for which we assess the predicted values, while the overbar indicates the mean over the number of observations for O_i and P_i. Contrary to the relative mismatches, in the NMSE the squared deviations (absolute values) are summed instead of the differences. For this reason, the NMSE generally shows the most striking differences among models. NMSE is a highly selective statistical quantity that can give large differences between models that perform similarly for other statistical measures. The lower the NMSE value, the better the performance of the model. On the other hand, high NMSE values do not necessarily mean that a model is completely wrong as the errors could be due to shifts in time and/or space. Moreover, it must be pointed out that NMSE is sensitive to outliers (Poli and Cirillo, 1993).

The calculated monthly average NMSE values for the 12 species using ECLIPSEv5 as the emission input can be seen in Figure 4 for year 2013–2015. The different scavenging coefficients used did not create a large variability in the monthly BC concentrations. This was caused due to the small perturbation of the scavenging coefficients. A more drastic change of wet scavenging would have caused BC concentrations to change more, as wet scavenging dominates removal and deposition of BC by approximately 80%. However, considering that the selection of the best representative species for BC was top priority, an effort to set realistic values to the scavenging coefficients was made. The best performance for the majority of the stations examined and most months was obtained for species 1, 2 and 10 (see Table 2). In terms of model response over the Arctic stations, a better performance was achieved for species 1 than for the other two. Therefore, we have chosen species 1 as our reference species for all subsequent analyses and the inversions. It should be noted here that the same test was performed using ACCMIPv5, EDGAR_HTAPv2.2 and MACCity emissions. Although the results were worse, the best-performed species for BC were again 1, 2 and 10.

3.2 Sensitivity to different prior information and selection of the best prior emission inventory

In this section we assess the impact of using the different prior emission inventories for BC and select the most appropriate one for our BC inversions. For this analysis, the best performing species 1 for BC (see Table 2) was chosen and the monthly relative model – observation mismatches (($[model - observations]/observations$) for all stations and years separated were calculated using all four inventories and are depicted in Figure S 3.

The largest monthly relative model-observation mismatches for the a priori simulated concentrations of BC in 2013 were calculated for stations located close to 50°N (BOS, CAB MEL, LEI, ULM, ANB). The average model-observation mismatch for all stations was 15% for 2013. Similar results were found for 2014 for the prior simulated BC concentrations with the largest relative mismatches recorded at mid-latitude stations where the BC concentrations were very high due to large anthropogenic emissions (BOS, CAB, MEL, LEI). On average, the relative model-observation mismatch was as high as 23% for the year 2014. Finally, in 2015, again the highest monthly relative mismatches of the a priori BC concentrations were estimated for the stations of high anthropogenic influence (CAB, MEL, LEI, WLD). The average relative model-observation mismatch in 2015 was only 19%, much lower than all previous years. The fact that all prior emission datasets used failed to reproduce the observations in central Europe during all years studied (2013, 2014 and 2015), whereas other stations at mid-latitudes were reproduced well, might imply either missing sources or highly uncertain measurements (Figure S 3). The use of different emission dataset changes simulated concentrations by a maximum of 23%.

Normalized mean square error (NMSE) values calculated for each of the four emission inventories were very low at the majority of the stations for which data existed in all the years of study (ZEP, SUM, TIK, BAR, MEL and LEI), when ECLIPSEv5 emissions were used. In contrast, at PAL all emission datasets performed well (Figure 5). The observations of BC concentrations at Arctic stations were better reproduced in simulations using the ECLIPSEv5 than with any other inventories examined. Law and Stohl (2007) have documented that these elevated BC concentrations are caused by anthropogenic emissions. Black carbon concentrations at TIK are not well simulated for reasons given in section 3.1.

3.3 Optimised (a posteriori) emissions of BC and associated uncertainty

The optimised annual emissions of BC together with the associated posterior gridded uncertainty and the difference between posterior and prior emissions averaged for the 2013–

364   2015 period can be seen in Figure 6. The posterior emissions are presented for the best

365   performing species (species 1) of BC and the best prior emissions inventory (ECLIPSEv5).

366   The total posterior uncertainty was calculated as the standard deviation of the posterior

367   emissions calculated for the 12 BC species with different scavenging coefficients for four

368   different emission datasets as prior information for each of the three years (12×4=48

369   inversions, see section 2.2). The total uncertainty is a propagation of the deposition

370   uncertainty (represented by the posterior emissions using 12 perturbed BC species with

371   different scavenging coefficients) and the uncertainty due to the use of different prior

372   information (represented by the posterior emissions using the four different emission

373   datasets). Table 3 reports annual prior, posterior, and averaged over 2013-2015, BC emissions

374   for different regions. Five different regions are accounted for, namely North America, North

375   Europe (including European Russia), North Siberia, Nenets-Komi (Russia) and Khanty-

376   Mansiysk district (Russia).

377   The optimised emissions show some constant hot-spot areas that persist throughout all

378   three years and which are attributed to anthropogenic BC emissions. For instance, emissions

379   in the Nenets – Komi region close to the Yamal peninsula in Russia or in Khanty Mansiysk

380   region of Northwestern Siberia have been reported to originate to a large extent from gas

381   flaring (Popovicheva et al., 2017; Stohl et al., 2013; Winiger et al., 2017). Other areas that are

382   characterised by large anthropogenic emissions are in Western Canada (Alberta), where more

383   than 100 power industries burn fossil fuels and more than 50 oil and gas production and oil

384   refining industries operate. In addition, one of the largest oil sands deposits are found in

385   Northern Alberta and in the McMurray area, which contains about 168 billion barrels of oil

386   (Heins, 2000). Cheng et al. (2018) found high concentrations of BC (more than 1000 ng m^{-3})

387   in the Canadian oil sands region at altitudes of up to 2 km during a flight campaign.

388   The optimised BC emissions in North America for the 2013–2015 period were between

389   149 and 193 kt y^{-1} (average ± 1-sigma error: 174±58 kt y^{-1}), in the same order with the prior

390   emissions in ECLIPSEv5 (148–182 kt y^{-1}) and slightly higher than ACCMIPv5,

391   EDGAR_HTAPv2.2 and MACCity (116–150 kt y^{-1}). In Northern Europe we estimated that

392   124–238 kt y^{-1} of BC were released (average ± 1-sigma error: 170±59 kt y^{-1}), which is less

393   than half the ECLIPSEv5 emissions (352–381 kt y^{-1}), about 35% lower than the ACCMIPv5

394   and MACCity emissions (241 – 256 kt y^{-1}) and in the same order as the EDGAR_HTAPv2.2

395   emissions (163–175 kt y^{-1}). Posterior BC emissions were higher in North Siberia for the 3-

396   year period (130–291 kt y^{-1}, average ± 1-sigma error: 217±69 kt y^{-1}) compared with

397   ECLIPSEv5 (187–238 kt y^{-1}), ACCMIPv5 (127–178 kt y^{-1}), EDGAR_HTAPv2.2 (108–159 kt

398   y^{-1}) or MACCity (129–179 kt y^{-1}). Larger changes in the BC emissions were calculated in

399   Russian territories that are known to be important gas flaring sources (Stohl et al., 2013). BC

400   emissions in the Nenets-Komi oblast were between 14 and 17 kt y^{-1} (average ± 1-sigma error:

401   15±5 kt y^{-1}), about 40% lower than the respective emissions in ECLIPSEv5 (≈25 kt y^{-1}), the

402   only prior dataset that took gas flaring into account there. This could be due to the decreasing

403   magnitude of the flaring emissions in the last few years (see Huang and Fu, 2016). Finally, in

404   Khanty-Mansiysk BC emissions were 28–37 kt y^{-1} (average ± 1-sigma error: 32±8 kt y^{-1})

405   compared to 25 kt yr^{-1} in ECLIPSEv5, whereas in the other datasets that do not include BC

406   emissions due to flaring, BC emissions were negligible. However, the posterior Khanty-

407   Mansiysk emissions are shifted further east compared to the prior.

408   The annual posterior BC emissions at latitudes above 50°N were estimated as 560±171

409   kt yr^{-1} averaged for the 2013–2015 time period (523±92 kt yr^{-1} in 2013, 608±104 kt yr^{-1} in

410   2014 and 549±100 kt yr^{-1} in 2015, respectively). For the same area and period, BC emissions

411   in ECLIPSEv5 were 745 kt yr^{-1}, in ACCMIPv5 533 kt yr^{-1}, in EDGAR_HTAPv2.2 437 kt yr^{-}

412   ^{1}, while in MACCity they were 538 kt yr^{-1}. The annual posterior absolute uncertainty can be

413   seen in Figure 6b. As it was explained before, this uncertainty is a combination of the

414   uncertainty due to scavenging and due to the use of different prior information in the

415   inversions of BC. Averaged over the period 2013-2015, the relative uncertainty of the

416   inversion was estimated to be 30%. The uncertainty due to different scavenging coefficients

417   in the BC species used was 25%, while the uncertainty due to the use of different prior

418   emissions was only 5%.

419   **3.4   Validation of the posterior emissions of BC**

420   The concentrations of BC at eight measurement stations simulated with the posterior

421   (optimised) BC emissions can be seen in Figure S 4. As expected, BC concentrations match

422   the observations significantly better than using any of the a priori datasets with correlation

423   coefficients above 0.6 for most of the stations. At the same time, NSD values were close to

424   unity or lower and the nRMSE values below 1.5 at most of the stations shown in Figure S 4.

425   However, the comparison to observations included in the inversion is not a sufficient

426   indicator of the inversion's performance, as the inversion is designed to reduce the model-

427   observation mismatches. The magnitude of the posterior reduction of the model mismatch to

428   the observations is partly determined by the weighting given to the observations relative to

429   the prior emissions. A much better performance indicator is the comparison of the posterior

concentrations with observations that were not included in the inversion (independent observations).

For this reason, we compared posterior BC concentrations with observations from the ACCACIA (Aerosol-Cloud Coupling and Climate Interactions in the Arctic) flight campaign, which was conducted near Zeppelin station, Ny-Ålesund, for 3 days in March 2013 (Sinha et al., 2017). This campaign was chosen because it was conducted during one year for which inversion results are available (2013). The results are shown in Figure 7 for the prior simulated concentrations of BC using four different emission datasets (ACCMIPv5, ECLIPSEv5, EDGAR_HTAPv2.2 and MACCity) and the posterior simulated BC concentrations. In all profiles, use of the optimised BC emissions results in a better agreement between modeled concentrations and observations compared to the prior simulated BC concentrations, while the RMSE (not normalised) values decrease substantially. However, the Pearson's correlation coefficients were below 0.5.

To assess the performance of the inversions of BC in 2014, we used an independent dataset from a ship campaign that took place in the North Atlantic and Baltic Seas in June and August 2014 (Figure 8) provided by Shevchenko et al. (2016). Although the measurements may sometimes be affected by the ship's exhaust, the posterior RMSE was 34% lower than the average RMSE using four different a priori emission datasets (ACCMIPv5, ECLIPSEv5, EDGAR_HTAPv2.2 and MACCity), supporting the view that the inversion improved the emissions for 2014.

To validate the 2015 inversions of BC, measurements from a ship campaign over the Russian Arctic were used (Popovicheva et al., 2017) and the results are shown in Figure 9. The cruise started from the port of Arkhangelsk in the Northwestern European Russia, reached the Bolshevik Island in the higher Russian Arctic and returned following more or less the same pathway. The calculated RMSE of the posterior BC concentrations with the measurements taken during the cruise was about 10% lower that the respective RMSE from the prior simulated concentrations of BC (average for all prior simulated emissions). This shows that the optimised emissions improved BC concentrations over the Russian Arctic. Some episodic peaks of BC throughout the ship cruise, however, were poorly captured.

4   Discussion

4.1 BC emissions in North America

The spatial distribution of the optimised BC emissions in North America averaged for the 3-year period is depicted in Figure 10 and the annual posterior emissions for 2013, 2014 and 2015 are shown in Figure S 5. The right panel of the same figures shows the differences between posterior and prior emissions (ECLIPSEv5) and highlights the biggest emission changes compared to the a priori dataset.

The most characteristic locations of sources between 2013 and 2015 lie in Alberta, where most of the large oil-producing industries operate (Figure 10 and Figure S 5). The highest emission source was located in 60°N–135°W in 2013 and 2015, but not in 2014. This spot corresponds to the location of Whitehorse, which is the capital and only city of Yukon, and the largest city in Northern Canada. The area involves mining activities (mainly for gold) and three natural gas wells, while biomass in the form of cordwood and pellets is used for space heating (Yukon Government, 2018). The fact that near-zero BC emissions were calculated in Whitehorse in 2014 might be due to the lack of available measurements in North America, which in turn results in poorly constrained posterior BC emissions. Another similar hotspot area that is more intense in 2013 and 2015, but not in 2014 is located in Yellowknife north of Great Slave Lake (62.5°N–115°W, Figure S 5). The city is known for gold and diamond mining and an oil-driven power plant (Northwest Territories Power Corporation, https://www.ntpc.com). Finally, another characteristic hotspot emission region of BC is seen southeast of Lake Athabasca (57°N–108°W, Figure 10). Uranium mines are located in this region. These mines use diesel generators, diesel trucks, and other diesel-powered machinery. Exactly in this location, the Visible Infrared Imaging Radiometer Suite (VIIRS) showed relatively strong night-time light sources (https://www.lightpollutionmap.info/#zoom=5&lat=8255540&lon=-11864816&layers=B0FFFTFFFT).

4.2 BC emissions in Northern Europe

The posterior BC emissions in Northern Europe averaged for the period 2013–2015 can be seen in Figure 11 together with the difference between prior (ECLIPSEv5) and posterior BC emissions, while the posterior emissions for each individual year are shown in Figure S 6. The location of the gas flaring facilities are also presented in the same figures together with vegetation fires from the FEINE (Fire Emission Inventory– northern Eurasia) inventory (Hao et al., 2016). The latter combines the MODIS thermal anomalies products (MOD14 and MYD14) and the MODIS top-of-the-atmosphere-calibrated reflectance product (MOD02) to

map and date burn scars that are screened for false detections. Land cover classification of burned areas are taken from the MODIS land cover change product (MOD12) (Friedl et al., 2010). This dataset is considered more realistic than GFED4 due to the emission factors used for BC (May et al., 2014) and the different approach of burned area calculation (see Hao et al., 2016).

The highest posterior BC emissions are calculated for the Moscow megacity at 55°N–37.5°E, Berlin 52°N–14°E, Warsaw 52°N–21°E, Kyiv 50°N–30°E, Saint Petersburg 60°N–30°E, while London is slightly misplaced to the west (Figure 11). The Scandinavian countries have the lowest emissions, although domestic heating there can also be important (Andersen and Jespersen, 2016). The difference between prior and posterior emissions show that vegetation fires have a large impact on the BC emissions especially in Eastern Europe. In particular in 2015, the inversion produces large emission increases exactly where a large number of fire hot spots were found (see Figure S 6).

4.3   BC emissions in North Siberia

Figure 12 illustrates the average posterior BC emissions in Western Siberia for the 2013–2015 period together with the difference between the prior (ECLIPSEv5) and the posterior BC emissions, while Figure S 7 shows the respective BC emissions for each year individually, together with the flaring facilities and the vegetation fires similarly to the previous section.

The prior BC emissions from flaring in Nenets-Komi oblast are confirmed by the inversion, although the emissions are shifted further east, while the flaring emissions in Khanty-Mansiysk are probably underestimated in ECLIPSEv5 (see also Table 3). Vegetation fires are shown to correlate well with BC emissions for 2013 (60°N –70°N) and 2014 (50°N–60°N) (Figure S 7), but not in 2015. Hotspots of high emissions were found in Dudinka (88°E–70°N), a town on the Yenisei River and the administrative center of Taymyrsky Dolgano-Nenetsky District of Krasnoyarsk Krai, Russia, due to the Norilsk Mining and Smelting Factory extracting coal and ores. Furthermore, increase posterior BC emissions were estimated across the line that connects some important Russian cities (Yekaterinburg to Chelyabinsk, 60°E–55°N). These cities have been reported to contribute large amounts of BC mainly from transportation (see Evangeliou et al., 2018). Another hotspot exists at 108°E–58°N that corresponds to VIIRS night-time lights (https://www.lightpollutionmap.info/#zoom=5.696666666666656&lat=8239438&lon=12096 227&layers=B0FFFTFFFT). These emissions are attributed to flaring as four facilities are

collocated there (see Figure 12). Finally, high BC emissions originate from the Nizhny Novgorod oblast (44°E–55°N). The oblast ranks seventh in Russia in industrial output. Processing industries predominate in the local economy. The leading sectors of more than 650 industries are engineering and metalworking, followed by chemical and petrochemical industries and forestry, woodworking, and paper industries and one facility that flare gas (GGFR, Figure 12).

In the western part of Siberia, there are numerous sources of average or low intensity. However, there no known anthropogenic sources there. At the lowest part of the inversion domain, in the borders of Russia with Mongolia, the posterior emissions showed a large increase (Figure 6). These emissions are prevalent along the Trans-Siberian Railway. Human activities in the villages along the railway have been highlighted to be the major cause of the fires there.

4.4 Seasonal variability of BC emissions

The monthly optimised BC emissions are shown in Figure 13 for the three years of study (2013–2015) for the entire area north of 50°N, and separately for areas north of 50°N in North America, North Europe, North Siberia, Nenets-Komi oblast (Russia) and Khanty-Mansiysk (Russia). The last two regions are known to have large emissions from gas flaring. In the same figure the prior emissions from ECLIPSEv5, EDGAR_HTAPv2.2, ACCMIPv5 and MACCity are plotted for comparison.

The total posterior BC emissions (>50°N) show large seasonal variation (Figure 13a). The maximum emissions were calculated for summer months (July in 2013 and June in 2014 and 2015). In these months large emissions from biomass burning have been reported both in GFED4 (see burned area in Giglio et al., 2013), as well as in the FEINE inventory for Northern Eurasia (Hao et al., 2016). Separating the inversion domain into continental regions reveals where biomass burning is important. For instance, in North America (Figure 13b), although GFED4 that is included in all the prior emission datasets, shows a large emission peak for BC in summer implying that fires are important, our optimised emissions show a significantly smaller variability. This was not the case for North Europe (Figure 13c) where the largest seasonal BC emissions were found in July for 2013 and in May for 2015, while in 2014 the largest peak appeared in April. This is not seen in the prior emission datasets, which show weak monthly variation. The largest seasonal variations were calculated for Northern Siberia (Figure 13d) and BC emissions there control the overall seasonal pattern for the total optimised BC emissions (>50°N). A large month-to-month variability was estimated in the

560 Nenets-Komi oblast (Figure 13e), but no clear seasonal pattern. Finally, the largest monthly

561 BC emissions in Khanty-Mansiysk oblast of Russia (Figure 13f) were calculated in April for

562 2013, July for 2014 and June for 2015 showing that a large share in the BC emissions in this

563 region originate from biomass burning since the region is located at mid-latitudes (60°N–

564 65°N) and is vulnerable to open fires.

565 **5   Conclusions**

566   We have optimised BC emissions at high northern latitudes (>50°N) for the 2013–2015

567 period using a Bayesian inversion tool, an atmospheric transport model and network of

568 continuous measurements of BC. We performed a sensitivity study to assess the best

569 representative species for BC according to the efficiency of in-cloud and below-cloud

570 scavenging, and the best representative emission inventory to be used as the prior information

571 for our inversion.

572   The perturbation of scavenging coefficients for BC in the simulated concentrations

573 creates a relative model–observation mismatch of 32%–43% for the three years of study,

574 whereas the use of different emission inventories has a less significant effect in the simulated

575 concentrations showing a relative model–observation mismatch of 15%–23%.

576   The posterior BC emissions show characteristic hot-spots throughout all three years in

577 the Nenets – Komi region close to the Yamal peninsula in Russia or in Khanty Mansiysk

578 region of Northwestern Siberia, where gas flaring facilities are located and in Western Canada

579 (Alberta), where more than 150 power and oil/gas production industries operate. The annual

580 posterior BC emissions at latitudes above 50°N were estimated as 560±171 kt yr^{-1},

581 significantly smaller than in ECLIPSEv5 (745 kt yr^{-1}), which was used and the prior

582 information in the inversions of BC (best representative emission dataset).

583   The uncertainty of the inversions was assessed using a model ensemble represented by

584 12 different scavenging coefficients for BC and four different prior emission datasets

585 (12×4=48) for each of the three years of our study. We calculate a relative uncertainty of the

586 inversion of 30% for the three years of our study.

587   The posterior simulated concentrations of BC showed a better agreement with

588 independent observations adopted from flight and ship campaigns over the Arctic presenting,

589 in all cases, up to three times lower RMSE values.

590   In North America, the posterior emissions were found similar to the a priori ones driven

591 by anthropogenic sources, while biomass burning appeared to be insignificant. This was

592 confirmed by satellite products that showed weak existence of active fire hot-spots.

593   In North Europe, posterior emissions were estimated to be half compared to the prior

594   ones, with the highest releases to be in megacities and due to biomass burning in Eastern

595   Europe.

596   Finally, in North Siberia the larger emissions were calculated along the transect

597   between Yekaterinburg and Chelyabinsk, while flaring in Nenets-Komi oblast is probably

598   overestimated in the a priori emissions. Increased emissions in the borders between Russia

599   and Mongolia are probably due to biomass burning in villages along the Trans-Siberian

600   Railway.

601

602   *Data availability.* All data generated for the present publication are stored on NIRD

603   (https://www.uio.no/english/services/it/research/storage/nird-sigma.html) (project NS9419K)

604   and can be obtained from the corresponding author upon request.

605

606   *Competing financial interests.* The authors declare no competing financial interests.

607

608   *Acknowledgements.* We would like to acknowledge the project entitled "Emissions of

609   Short-Lived Climate Forcers near and in the Arctic (SLICFONIA)", which was funded by the

610   NORRUSS research program (Project ID: 233642) and the project entitled "The Role of

611   Short-Lived Climate Forcers in the Global Climate" funded by the KLIMAFORSK program

612   (Project ID: 235548) of the Research Council of Norway. Also the Research Council of

613   Norway strategic institute initiatives (SIS) project "SOCA-Signals from the Arctic OCean in

614   the Atmosphere" is acknowledged. We also acknowledge partial support by the AMAP

615   secretariat, as this work shall contribute to the next AMAP assessment on short-lived climate

616   forcers. Work was performed at the Nordic Centre of Excellence eSTICC (eScience Tools for

617   Investigating Climate Change in northern high latitudes), supported by NordForsk grant

618   57001. We thank IIASA (especially Chris Heyes and Zig Klimont) for providing the

619   ECLIPSEv5 emission dataset for BC. Computational and storage resources for the

620   FLEXPART simulations were provided by NOTUR (NN9419K) and NIRD (NS9419K). All

621   results can be accessed upon request to the corresponding author of this manuscript.

622

623   *Author contributions.* NE performed the simulations, analyses and wrote the paper, RLT

624   helped in the adaptation of FLEXINVERT for BC and commented on the paper, SE helped in

625   the implementation of the experiments and AS coordinated, commented and wrote parts of

626   the paper.

627

References

629 Ackerman, a. S.: Reduction of Tropical Cloudiness by Soot, Science (80-.)., 288(5468),

630 1042–1047, doi:10.1126/science.288.5468.1042, 2000.

631 AMAP: AMAP assessment 2015: Black carbon and ozone as Arctic climate forcers, Arctic

632 Monitoring and Assessment Programme (AMAP), Oslo, Norway., 2015.

633 Andersen, S. and Jespersen, M. G.: A Protocol for Measuring Emissions of Black Carbon and

634 Organic Carbon from Residential Wood Burning. [online] Available from:

635 http://webcache.googleusercontent.com/search?q=cache:T48eUfM_V6YJ:www.ccacoalition.

636 org/en/file/2570/download%3Ftoken%3DNkBK2GWw+&cd=3&hl=no&ct=clnk&gl=no&cli

637 ent=safari, 2016.

638 Asmi, E., Kondratyev, V., Brus, D., Laurila, T., Lihavainen, H., Backman, J., Vakkari, V.,

639 Aurela, M., Hatakka, J., Viisanen, Y., Uttal, T., Ivakhov, V. and Makshtas, A.: Aerosol size

640 distribution seasonal characteristics measured in Tiksi, Russian Arctic, Atmos. Chem. Phys.,

641 16(3), 1271–1287, doi:10.5194/acp-16-1271-2016, 2016.

642 Benkovitz, C. M., Schwartz, S. E., Jensen, M. P., Miller, M. A., Easter, R. C. and Bates, T. S.:

643 Modeling atmospheric sulfur over the Northern Hemisphere during the Aerosol

644 Characterization Experiment 2 experimental period, J. Geophys. Res. D Atmos., 109(22), 1–

645 28, doi:10.1029/2004JD004939, 2004.

646 Bond, T. C. and Bergstrom, R. W.: Light Absorption by Carbonaceous Particles: An

647 Investigative Review, Aerosol Sci. Technol., 40(1), 27–67, doi:10.1080/02786820500421521,

648 2006.

649 Bond, T. C., Streets, D. G., Yarber, K. F., Nelson, S. M., Woo, J. H. and Klimont, Z.: A

650 technology-based global inventory of black and organic carbon emissions from combustion, J.

651 Geophys. Res. D Atmos., 109(14), 1–43, doi:10.1029/2003JD003697, 2004.

652 Bond, T. C., Doherty, S. J., Fahey, D. W., Forster, P. M., Berntsen, T., Deangelo, B. J.,

653 Flanner, M. G., Ghan, S., Kärcher, B., Koch, D., Kinne, S., Kondo, Y., Quinn, P. K., Sarofim,

654 M. C., Schultz, M. G., Schulz, M., Venkataraman, C., Zhang, H., Zhang, S., Bellouin, N.,

655 Guttikunda, S. K., Hopke, P. K., Jacobson, M. Z., Kaiser, J. W., Klimont, Z., Lohmann, U.,

656 Schwarz, J. P., Shindell, D., Storelvmo, T., Warren, S. G. and Zender, C. S.: Bounding the

657 role of black carbon in the climate system: A scientific assessment, J. Geophys. Res. Atmos.,

658 118(11), 5380–5552, doi:10.1002/jgrd.50171, 2013.

659 Browse, J., Carslaw, K. S., Arnold, S. R., Pringle, K. and Boucher, O.: The scavenging

660 processes controlling the seasonal cycle in Arctic sulphate and black carbon aerosol, Atmos.

Chem. Phys., 12(15), 6775–6798, doi:10.5194/acp-12-6775-2012, 2012.

Brunner, D., Arnold, T., Henne, S., Manning, A., Thompson, R. L., Maione, M., Doherty, S. O. and Reimann, S.: Comparison of four inverse modelling systems applied to the estimation of HFC-125 , HFC-134a , and SF 6 emissions over Europe, , 10651–10674, 2017.

Cao, G., Zhang, X. and Zheng, F.: Inventory of black carbon and organic carbon emissions from China, Atmos. Environ., 40(34), 6516–6527, doi:10.1016/j.atmosenv.2006.05.070, 2006.

Cheng, Y., Li, S., Gordon, M. and Liu, P.: Size distribution and coating thickness of black carbon from the Canadian oil sands operations, , 2004, 2653–2667, 2018.

Clarke, A. D. and Noone, K. J.: Soot in the arctic snowpack: a cause for perturbations in radiative transfer, Atmos. Environ., 41(SUPPL.), 64–72, doi:10.1016/0004-6981(85)90113-1, 1985.

Eckhardt, S., Quennehen, B., Olivié, D. J. L., Berntsen, T. K., Cherian, R., Christensen, J. H., Collins, W., Crepinsek, S., Daskalakis, N., Flanner, M., Herber, A., Heyes, C., Hodnebrog, Huang, L., Kanakidou, M., Klimont, Z., Langner, J., Law, K. S., Lund, M. T., Mahmood, R., Massling, A., Myriokefalitakis, S., Nielsen, I. E., Nøjgaard, J. K., Quaas, J., Quinn, P. K., Raut, J. C., Rumbold, S. T., Schulz, M., Sharma, S., Skeie, R. B., Skov, H., Uttal, T., Von Salzen, K. and Stohl, A.: Current model capabilities for simulating black carbon and sulfate concentrations in the Arctic atmosphere: A multi-model evaluation using a comprehensive measurement data set, Atmos. Chem. Phys., 15(16), 9413–9433, doi:10.5194/acp-15-9413-2015, 2015.

Elvidge, C. D., Ziskin, D., Baugh, K. E., Tuttle, B. T., Ghosh, T., Pack, D. W., Erwin, E. H. and Zhizhin, M.: A fifteen year record of global natural gas flaring derived from satellite data, Energies, 2(3), 595–622, doi:10.3390/en20300595, 2009.

Evangeliou, N., Balkanski, Y., Hao, W. M., Petkov, A., Silverstein, R. P., Corley, R., Nordgren, B. L., Urbanski, S. P., Eckhardt, S., Stohl, A., Tunved, P., Crepinsek, S., Jefferson, A., Sharma, S., Nøjgaard, J. K. and Skov, H.: Wildfires in northern Eurasia affect the budget of black carbon in the Arctic-a 12-year retrospective synopsis (2002-2013), Atmos. Chem. Phys., 16(12), 7587–7604, doi:10.5194/acp-16-7587-2016, 2016.

Evangeliou, N., Shevchenko, V. P., Yttri, K. E., Sollum, E., Pokrovsky, O. S., Kobelev, V. O., Vladimir, B., Lobanov, A. A., Starodymova, D. P., Vorobiev, S. N., Thompson, R. L., Stohl, A., Toulouse, G. E. and Belin, E.: Origin of elemental carbon in snow from Western Siberia and northwestern European Russia during winter – spring, Atmos. Chem. Phys., 18, 963–977, doi:10.5194/acp-18-963-2018, 2018.

695 Friedl, M. A., Sulla-Menashe, D., Tan, B., Schneider, A., Ramankutty, N., Sibley, A. and

696 Huang, X.: MODIS Collection 5 global land cover: Algorithm refinements and

697 characterization of new datasets, Remote Sens. Environ., 114(1), 168–182,

698 doi:10.1016/j.rse.2009.08.016, 2010.

699 Gelencsér, A., Hoffer, A., Molnár, A., Krivácsy, Z., Kiss, G. and Mészáros, E.: Thermal

700 behaviour of carbonaceous aerosol from a continental background site, Atmos. Environ.,

701 34(5), 823–831, doi:10.1016/S1352-2310(99)00206-X, 2000.

702 Giglio, L., Randerson, J. T. and van der Werf, G. R.: Analysis of daily, monthly, and annual

703 burned area using the fourth-generation global fire emissions database (GFED4), J. Geophys.

704 Res. Biogeosciences, 118, 317–328, doi:10.1002/jgrg.20042, 2013, 2013.

705 Government, Y.: Economic sectors, 2018.

706 Grythe, H., Kristiansen, N. I., Groot Zwaaftink, C. D., Eckhardt, S., Ström, J., Tunved, P.,

707 Krejci, R. and Stohl, A.: A new aerosol wet removal scheme for the Lagrangian particle

708 model FLEXPARTv10, Geosci. Model Dev., 10, 1447–1466, doi:10.5194/gmd-10-1447-

709 2017, 2017.

710 Hao, W. M., Petkov, A., Nordgren, B. L., Silverstein, R. P., Corley, R. E., Urbanski, S. P.,

711 Evangeliou, N., Balkanski, Y. and Kinder, B.: Daily black carbon emissions from fires in

712 Northern Eurasia from 2002 to 2013, Geosci. Model Dev., 9, 4461–4474, doi:10.5194/gmd-9-

713 4461-2016, 2016.

714 Hegg, D. A., Warren, S. G., Grenfell, T. C., Doherty, S. J., Larson, T. V. and Clarke, A. D.:

715 Source attribution of black carbon in arctic snow, Environ. Sci. Technol., 43(11), 4016–4021,

716 doi:10.1021/es803623f, 2009.

717 Heins, F. J.: Historical overview of the Fort McMurray area and oil sands industry in

718 Northeast Alberta. [online] Available from:

719 https://web.archive.org/web/20080227201038/http://www.ags.gov.ab.ca/publications/ESR/P

720 DF/ESR_2000_05.pdf, 2000.

721 Hodnebrog, Ø., Myhre, G. and Samset, B. H.: How shorter black carbon lifetime alters its

722 climate effect., Nat. Commun., 5(May), 5065, doi:10.1038/ncomms6065, 2014.

723 Huang, K. and Fu, J. S.: A global gas flaring black carbon emission rate dataset from 1994 to

724 2012, Nature, 3, 160104, doi:10.1038/sdata.2016.104, 2016.

725 Huang, K., Fu, J. S., Prikhodko, V. Y., Storey, J. M., Romanov, A., Hodson, E. L., Cresko, J.,

726 Morozova, I., Ignatieva, Y. and Cabaniss, J.: Russian anthropogenic black carbon: Emission

727 reconstruction and Arctic black carbon simulation, J. Geophys. Res. Atmos., 120(21), 11306–

728 11333, doi:10.1002/2015JD023358, 2015.

729 Janssens-Maenhout, G., Crippa, M., Guizzardi, D., Dentener, F., Muntean, M., Pouliot, G.,

730 Keating, T., Zhang, Q., Kurokawa, J., Wankmüller, R., Denier Van Der Gon, H., Kuenen, J. J.

731 P., Klimont, Z., Frost, G., Darras, S., Koffi, B. and Li, M.: HTAP-v2.2: A mosaic of regional

732 and global emission grid maps for 2008 and 2010 to study hemispheric transport of air

733 pollution, Atmos. Chem. Phys., 15(19), 11411–11432, doi:10.5194/acp-15-11411-2015, 2015.

734 Jinhuan, Q. and Liquan, Y.: Variation characteristics of atmospheric aerosol optical depths

735 and visibility in North China during 1980 } 1994, Atmos. Environ., 34, 603–609, 2000.

736 Klimont, Z., Kupiainen, K., Heyes, C., Purohit, P., Cofala, J., Rafaj, P., Borken-Kleefeld, J.

737 and Schöpp, W.: Global anthropogenic emissions of particulate matter including black

738 carbon, Atmos. Chem. Phys., 17, 8681–8723, doi:10.5194/acp-17- 50 8681-2017, 2017.

739 Klonecki, A.: Seasonal changes in the transport of pollutants into the Arctic troposphere-

740 model study, J. Geophys. Res., 108(D4), 8367, doi:10.1029/2002JD002199, 2003.

741 Koch, D. and Hansen, J.: Distant origins of Arctic black carbon: A Goddard Institute for

742 Space Studies ModelE experiment, J. Geophys. Res. D Atmos., 110(4), 1–14,

743 doi:10.1029/2004JD005296, 2005.

744 Lamarque, J. F., Bond, T. C., Eyring, V., Granier, C., Heil, A., Klimont, Z., Lee, D., Liousse,

745 C., Mieville, A., Owen, B., Schultz, M. G., Shindell, D., Smith, S. J., Stehfest, E., Van

746 Aardenne, J., Cooper, O. R., Kainuma, M., Mahowald, N., McConnell, J. R., Naik, V., Riahi,

747 K. and Van Vuuren, D. P.: Historical (1850-2000) gridded anthropogenic and biomass

748 burning emissions of reactive gases and aerosols: Methodology and application, Atmos.

749 Chem. Phys., 10(15), 7017–7039, doi:10.5194/acp-10-7017-2010, 2010.

750 Lamarque, J. F., Shindell, D. T., Josse, B., Young, P. J., Cionni, I., Eyring, V., Bergmann, D.,

751 Cameron-Smith, P., Collins, W. J., Doherty, R., Dalsoren, S., Faluvegi, G., Folberth, G.,

752 Ghan, S. J., Horowitz, L. W., Lee, Y. H., MacKenzie, I. A., Nagashima, T., Naik, V.,

753 Plummer, D., Righi, M., Rumbold, S. T., Schulz, M., Skeie, R. B., Stevenson, D. S., Strode,

754 S., Sudo, K., Szopa, S., Voulgarakis, A. and Zeng, G.: The atmospheric chemistry and climate

755 model intercomparison Project (ACCMIP): Overview and description of models, simulations

756 and climate diagnostics, Geosci. Model Dev., 6(1), 179–206, doi:10.5194/gmd-6-179-2013,

757 2013.

758 Law, K. S. and Stohl, A.: Arctic Air Pollution: Origins and Impacts, Science (80-.).,

759 315(5818), 1537–1540, doi:10.1126/science.1137695, 2007.

760 Long, C. M., Nascarella, M. A. and Valberg, P. A.: Carbon black vs. black carbon and other

761 airborne materials containing elemental carbon: Physical and chemical distinctions, Environ.

762 Pollut., 181, 271–286, doi:10.1016/j.envpol.2013.06.009, 2013.

763   May, A. A., McMeeking, G. R., Lee, T., Taylor, J. W., Craven, J. S., Burling, I., Sullivan1, A.

764   P., Akagi, S., Jr., J. L. C., Flynn, M., Coe, H., Urbanski, S. P., Seinfeld6, J. H., Yokelson8, R.

765   J. and Kreidenweis, S. M.: Aerosol emissions from prescribed fires in the United States: A

766   synthesis of laboratory and aircraft measurements, J. Geophys. Res. Atmos., 119, 11826–

767   11849, doi:10.1002/ 2014JD021848, 2014.

768   Muller, T., Henzing, J. S., De Leeuw, G., Wiedensohler, A., Alastuey, A., Angelov, H.,

769   Bizjak, M., Collaud Coen, M., Engstr??m, J. E., Gruening, C., Hillamo, R., Hoffer, A., Imre,

770   K., Ivanow, P., Jennings, G., Sun, J. Y., Kalivitis, N., Karlsson, H., Komppula, M., Laj, P., Li,

771   S. M., Lunder, C., Marinoni, A., Martins Dos Santos, S., Moerman, M., Nowak, A., Ogren, J.

772   A., Petzold, A., Pichon, J. M., Rodriquez, S., Sharma, S., Sheridan, P. J., Teinil??, K., Tuch,

773   T., Viana, M., Virkkula, A., Weingartner, E., Wilhelm, R. and Wang, Y. Q.: Characterization

774   and intercomparison of aerosol absorption photometers: Result of two intercomparison

775   workshops, Atmos. Meas. Tech., 4(2), 245–268, doi:10.5194/amt-4-245-2011, 2011.

776   Myhre, G., Samset, B. H., Schulz, M., Balkanski, Y., Bauer, S., Berntsen, T. K., Bian, H.,

777   Bellouin, N., Chin, M., Diehl, T., Easter, R. C., Feichter, J., Ghan, S. J., Hauglustaine, D.,

778   Iversen, T., Kinne, S., Kirkeväg, A., Lamarque, J. F., Lin, G., Liu, X., Lund, M. T., Luo, G.,

779   Ma, X., Van Noije, T., Penner, J. E., Rasch, P. J., Ruiz, A., Seland, Skeie, R. B., Stier, P.,

780   Takemura, T., Tsigaridis, K., Wang, P., Wang, Z., Xu, L., Yu, H., Yu, F., Yoon, J. H., Zhang,

781   K., Zhang, H. and Zhou, C.: Radiative forcing of the direct aerosol effect from AeroCom

782   Phase II simulations, Atmos. Chem. Phys., 13(4), 1853–1877, doi:10.5194/acp-13-1853-2013,

783   2013.

784   Nordmann, S., Birmili, W., Weinhold, K., Müller, K., Spindler, G. and Wiedensohler, A.:

785   Measurements of the mass absorption cross section of atmospheric soot particles using

786   Raman spectroscopy, J. Geophys. Res. Atmos., 118(21), 12075–12085,

787   doi:10.1002/2013JD020021, 2013.

788   Park, R. J., Jacob, D. J., Palmer, P. I., Clarke, A. D., Weber, R. J., Zondlo, M. A., Eisele, F.

789   L., Bandy, A. R., Thornton, D. C., Sachse, G. W. and Bond, T. C.: Export efficiency of black

790   carbon aerosol in continental outflow: Global implications, J. Geophys. Res. D Atmos.,

791   110(11), 1–7, doi:10.1029/2004JD005432, 2005.

792   Petzold, A. and Schönlinner, M.: Multi-angle absorption photometry - A new method for the

793   measurement of aerosol light absorption and atmospheric black carbon, J. Aerosol Sci., 35(4),

794   421–441, doi:10.1016/j.jaerosci.2003.09.005, 2004.

795   Petzold, A., Ogren, J. A., Fiebig, M., Laj, P., Li, S. M., Baltensperger, U., Holzer-Popp, T.,

796   Kinne, S., Pappalardo, G., Sugimoto, N., Wehrli, C., Wiedensohler, A. and Zhang, X. Y.:

797 Recommendations for reporting black carbon measurements, Atmos. Chem. Phys., 13(16),

798 8365–8379, doi:10.5194/acp-13-8365-2013, 2013.

799 Poli, A. A. and Cirillo, M. C.: On the use of the normalized mean square error in evaluating

800 dispersion model performance, Atmos. Environ. Part A, Gen. Top., 27(15), 2427–2434,

801 doi:10.1016/0960-1686(93)90410-Z, 1993.

802 Popovicheva, O. B., Evangeliou, N., Eleftheriadis, K., Kalogridis, A. C., Movchan, V.,

803 Sitnikov, N., Eckhardt, S., Makshtas, A. and Stohl, A.: Black carbon sources constrained by

804 observations and modeling in the Russian high Arctic, Environ. Sci. Technol., 51,

805 3871−3879, doi:10.1021/acs.est.6b05832, 2017.

806 Samset, B. H., Myhre, G., Herber, A., Kondo, Y., Li, S. M., Moteki, N., Koike, M., Oshima,

807 N., Schwarz, J. P., Balkanski, Y., Bauer, S. E., Bellouin, N., Berntsen, T. K., Bian, H., Chin,

808 M., Diehl, T., Easter, R. C., Ghan, S. J., Iversen, T., Kirkev??g, A., Lamarque, J. F., Lin, G.,

809 Liu, X., Penner, J. E., Schulz, M., Seland, Skeie, R. B., Stier, P., Takemura, T., Tsigaridis, K.

810 and Zhang, K.: Modelled black carbon radiative forcing and atmospheric lifetime in AeroCom

811 Phase II constrained by aircraft observations, Atmos. Chem. Phys., 14(22), 12465–12477,

812 doi:10.5194/acp-14-12465-2014, 2014.

813 Schaap, M., Denier Van Der Gon, H. A. C., Dentener, F. J., Visschedijk, A. J. H., Van Loon,

814 M., ten Brink, H. M., Putaud, J. P., Guillaume, B., Liousse, C. and Builtjes, P. J. H.:

815 Anthropogenic black carbon and fine aerosol distribution over Europe, J. Geophys. Res.

816 Atmos., 109(18), doi:10.1029/2003JD004330, 2004.

817 Schladitz, A., Leníček, J., Beneš, I., Kováč, M., Skorkovský, J., Soukup, A., Jandlová, J.,

818 Poulain, L., Plachá, H., Löschau, G. and Wiedensohler, A.: Air quality in the German-Czech

819 border region: A focus on harmful fractions of PM and ultrafine particles, Atmos. Environ.,

820 122, 236–249, doi:10.1016/j.atmosenv.2015.09.044, 2015.

821 Seibert, P. and Frank, A.: Source-receptor matrix calculation with a Lagrangian particle

822 dispersion model in backward mode, Atmos. Chem. Phys., 4(1), 51–63, doi:10.5194/acp-4-

823 51-2004, 2004.

824 Shevchenko, V. P., Kopeikin, V. M., Evangeliou, N., Lisitzin, A. P., Novigatsky, A. N.,

825 Pankratova, N. V, Starodymova, D. P., Stohl, A. and Thompson, R.: Atmospheric Black

826 Carbon over the North Atlantic and the Russian Arctic Seas in Summer-Autumn Time,

827 Химия В Интересах Устойчивого Развития, 24(4), 441–446,

828 doi:10.15372/KhUR20160402, 2016.

829 Sinha, P. R., Kondo, Y., Koike, M., Ogren, J. A., Jefferson, A., Barrett, T. E., Sheesley, R. J.,

830 Ohata, S., Moteki, N., Coe, H., Liu, D., Irwin, M., Tunved, P., Quinn, P. K. and Zhao, Y.:

Evaluation of ground-based black carbon measurements by filter-based photometers at two

Arctic sites, J. Geophys. Res., 122(6), 3544–3572, doi:10.1002/2016JD025843, 2017.

Slinn, W. G. N.: Predictions for particle deposition to vegetative canopies, Atmos. Environ.,

16, 1785–1794, doi:10.1016/0004-6981(82)90271-2, 1982.

Stohl, A.: Characteristics of atmospheric transport into the Arctic troposphere, J. Geophys.

Res. Atmos., 111(11), 1–17, doi:10.1029/2005JD006888, 2006.

Stohl, A., Hittenberger, M. and Wotawa, G.: Validation of the lagrangian particle dispersion

model FLEXPART against large-scale tracer experiment data, Atmos. Environ., 32(24),

4245–4264, doi:10.1016/S1352-2310(98)00184-8, 1998.

Stohl, A., Forster, C., Frank, A., Seibert, P. and Wotawa, G.: Technical note: The Lagrangian

particle dispersion model FLEXPART version 6.2, Atmos. Chem. Phys., 5(9), 2461–2474,

doi:10.5194/acp-5-2461-2005, 2005.

Stohl, A., Seibert, P., Arduini, J., Eckhardt, S., Fraser, P., Greally, B. R., Maione, M.,

O'Doherty, S., Prinn, R. G., Reimann, S., Saito, T., Schmidbauer, N., Simmonds, P. G.,

Vollmer, M. K., Weiss, R. F. and Yokouchi, Y.: A new analytical inversion method for

determining regional and global emissions of greenhouse gases: sensitivity studies and

application to halocarbons, Atmos. Chem. Phys., 9, 1597–1620, doi:10.5194/acp-9-1597-

2009, 2009.

Stohl, A., Klimont, Z., Eckhardt, S., Kupiainen, K., Shevchenko, V. P., Kopeikin, V. M. and

Novigatsky, A. N.: Black carbon in the Arctic: The underestimated role of gas flaring and

residential combustion emissions, Atmos. Chem. Phys., 13(17), 8833–8855, doi:10.5194/acp-

13-8833-2013, 2013.

Streets, D. G., Bond, T. C., Carmichael, G. R., Fernandes, S. D., Fu, Q., He, D., Klimont, Z.,

Nelson, S. M., Tsai, N. Y., Wang, M. Q., Woo, J.-H. and Yarber, K. F.: An inventory of

gaseous and primary aerosol emissions in Asia in the year 2000, J. Geophys. Res., 108(D21),

8809, doi:10.1029/2002JD003093, 2003.

Tarantola, A.: Inverse Problem Theory and Methods for Model Parameter Estimation, Society

for Industrial and Applied Mathematics, Philadelphia, Pa., 2005.

Textor, C., Schulz, M., Guibert, S., Kinne, S., Balkanski, Y., Bauer, S., Berntsen, T., Berglen,

T., Boucher, O., Chin, M., Dentener, F., Diehl, T., Easter, R., Feichter, H., Fillmore, D.,

Ghan, S., Ginoux, P., Gong, S., Grini, a., Hendricks, J., Horowitz, L., Huang, P., Isaksen, I.,

Iversen, T., Kloster, S., Koch, D., Kirkevåg, a., Kristjansson, J. E., Krol, M., Lauer, a.,

Lamarque, J. F., Liu, X., Montanaro, V., Myhre, G., Penner, J., Pitari, G., Lamarque, J. F.,

Liu, X., Montanaro, V., Myhre, G., Penner, J., Pitari, G., Reddy, S., Seland, Ø., Stier, P.,

865 Takemura, T. and Tie, X.: Analysis and quantification of the diversities of aerosol life cycles

866 within AeroCom, Atmos. Chem. Phys., 6, 1777–1813, doi:10.5194/acpd-5-8331-2005, 2006.

867 Thacker, W. C.: Data assimilation with inequality constraints, Ocean Model., 16(3–4), 264–

868 276, doi:10.1016/j.ocemod.2006.11.001, 2007.

869 Thompson, R. L. and Stohl, A.: FLEXINVERT: An atmospheric Bayesian inversion

870 framework for determining surface fluxes of trace species using an optimized grid, Geosci.

871 Model Dev., 7(5), 2223–2242, doi:10.5194/gmd-7-2223-2014, 2014.

872 Thompson, R. L., Stohl, A., Zhou, L. X., Dlugokencky, E., Fukuyama, Y., Tohjima, Y., Kim,

873 S. Y., Lee, H., Nisbet, E. G., Fisher, R. E., Lowry, D., Weiss, R. F., Prinn, R. G., O'Doherty,

874 S., Young, D. and White, J. W. C.: Methane emissions in East Asia for 2000-2011 estimated

875 using an atmospheric Bayesian inversion, J. Geophys. Res. Atmos., 120(9), 4352–4369,

876 doi:10.1002/2014JD022394, 2015.

877 Thompson, R. L., Sasakawa, M., Machida, T., Aalto, T., Worthy, D., Lavric, J. V., Lund

878 Myhre, C. and Stohl, A.: Methane fluxes in the high northern latitudes for 2005-2013

879 estimated using a Bayesian atmospheric inversion, Atmos. Chem. Phys., 17, 3553–3572,

880 doi:10.5194/acp-17-3553-2017, 2017.

881 Wang, P., Wang, H., Wang, Y. Q., Zhang, X. Y., Gong, S. L., Xue, M., Zhou, C. H., Liu, H.

882 L., An, X. Q., Niu, T. and Cheng, Y. L.: Inverse modeling of black carbon emissions over

883 China using ensemble data assimilation, Atmos. Chem. Phys., 16(2), 989–1002,

884 doi:10.5194/acp-16-989-2016, 2016.

885 Wang, R., Tao, S., Balkanski, Y., Ciais, P., Boucher, O., Liu, J., Piao, S., Shen, H., Vuolo, M.

886 R., Valari, M., Chen, H., Chen, Y., Cozic, A., Huang, Y., Li, B., Li, W., Shen, G., Wang, B.

887 and Zhang, Y.: Exposure to ambient black carbon derived from a unique inventory and high-

888 resolution model., Proc. Natl. Acad. Sci. U. S. A., 111(7), 2459–63,

889 doi:10.1073/pnas.1318763111, 2014.

890 Winiger, P., Andersson, A., Eckhardt, S., Stohl, A., Semiletov, I. P., Dudarev, O. V., Charkin,

891 A., Shakhova, N., Klimont, Z., Heyes, C. and Gustafsson, Ö.: Siberian Arctic black carbon

892 sources constrained by model and observation, Proc. Natl. Acad. Sci., 114(7), E1054–E1061,

893 doi:10.1073/pnas.1613401114, 2017.

894

TABLES & LEGENDS

Table 1. Observation sites used for the inversions (the altitude indicates the sampling height in meters above sea level).

Site ID	Organisation	Latitude	Longitude	Altitude	Year	Instrument	Description
ALT	EC/AES	82.5°N	62.5°W	205 m	2013, 2015	PSAP-3W	Alert, Nunavut, Canada
ANB	HMGU	50.6°N	13.0°E	549 m	2013	MAAP	Annaberg-Buchholz, Germany
APP	AAIRF	36.2°N	81.7°W	1110 m	2015	PSAP-3W	Appalachian SU, Boone, USA
ASP	SU	58.8°N	17.4°E	20 m	2013	PSAP	Asprveten, Västerås, Sweden
BAR	NOAA-ESRL	71.3°N	161.6°W	9 m	2013, 2014, 2015	CLAP-3W	Barrow, Alaska, USA
BIR	NILU	58.4°N	8.2°E	219 m	2014, 2015	PSAP-3W	Birkenes, Norway
BON	NOAA-ESRL	40.0°N	88.4°W	213	2015	CLAP-3W	Bondville, USA
BOS	TROPOS	53.0°N	7.9°E	53 m	2013, 2014	MAAP-5012	Bösel, Germany
CAB	ACTRIS, GAW	52.0°N	4.9°E	61 m	2013, 2014, 2015	Thermo-5012	Cabauw Zijdeweg, Netherlands
COL	NOAA-ESRL	40.4°N	106.7°W	3220 m	2015	PSAP-3W	Steamboat Springs, Colorado, USA
ETL	EC/AES	54.4°N	105.0°W	502 m	2013, 2015	PSAP-1W	East Trout Lake, Canada
GOS	NOAA	33.3°N	126.2°E	72 m	2014, 2015	CLAP-3W	Gosan, South Korea
HYY	UH, DPS	61.6°N	24.2°E	181 m	2013, 2015	Thermo-5012	Hyytiälä, Finland
KPU	HMS, ACUV	47.0°N	19.6°E	125 m	2013, 2014, 2015	CLAP-3W	K-puszta, Hungary
LEI	TROPOS	51.3°N	12.3°E	122 m	2013, 2014, 2015	MAAP-5012	Leipzig, Germany
MEL	TROPOS	51.5°N	12.9°E	86 m	2013, 2014, 2015	MAAP-5012	Melpitz, Torgau, Germany
MOU	ACTRIS, GAW	42.2°N	23.6°E	2971 m	2014, 2015	CLAP-3W	BEO Moussala, Bulgaria
MOV	-	38.1°N	8.8°W	43 m	2015	RFPS-1287	Monte Velho, Portugal
NEP	CNR	28.0°N	86.8°E	5079 m	2015	MAAP01	Nepal Climate Observatory
PAL	FMI	68.0°N	24.2°E	560 m	2013, 2014, 2015	Thermo-5012	Pallas, Sodankylä, Finland
SGP	NOAA-ESRL	36.6°N	97.5°W	318 m	2015	PSAP-3W	South Great Planes, USA
SUM	PF	72.6°N	38.5°W	3211 m	2013, 2014, 2015	CLAP-3W	Summit, Greenland
TIK	NOAA, MeteoRF	71.6°N	128.9°E	30 m	2013, 2014, 2015	Magee AE31	Tiksi, Russian Federation
TRI	NOAA-ESRL	41.1°N	124.2°W	117 m	2015	PSAP-3W	Trinidad Head, Canada
ULM	ACTRIS, GAW	50.7°N	14.8°E	161 m	2013	MAAP-CHMI	Ústí n.L.-mesto, Czechia
WHI	EC/AES	50.0°N	122.9°W	2182 m	2013, 2015	PSAP-1W	Whisper, British Columbia, Canada
WLD	GAW-WDCA	52.8°N	10.8°E	78 m	2015	MAAP-5012	Waldhof, Germany
ZEP	NCSRD	78.9°N	11.9°E	474 m	2013, 2014, 2015	Magee AE31	Zeppelin, Ny Ålesund, Norway

897   **Table 2.** Different scavenging parameters of below–cloud and in–cloud scavenging used in the ensemble model simulations for BC. A and B are

898   rain and snow collection efficiencies for below-cloud scavenging, A_i is the cloud condensation nuclei efficiency and B_i the ice nuclei efficiency

899   that are used in in-cloud scavenging following Grythe et al. (2017).

	A	B	A_i	B_i
BC1	1.0	1.0	0.90	0.10
BC2	1.0	1.0	0.90	0.45
BC3	1.0	1.0	0.45	0.20
BC4	1.0	0.5	0.45	0.20
BC5	0.5	0.5	0.45	0.20
BC6	1.0	0.2	0.90	0.20
BC7	1.0	1.0	0.20	0.20
BC8	2.0	1.0	0.45	0.10
BC9	0.2	0.2	0.90	0.90
BC10	1.0	1.0	0.90	0.20
BC11	2.0	1.0	0.45	0.45
BC12	1.0	1.0	0.45	0.00

900

901
902
903
904
905

Table 3. Annual prior (ACCMIPv5, EDGAR_HTAPv2.2, MACCity and ECLIPSEv5) and posterior emissions of BC for 2013, 2014 and 2015 (inversion using best representative species and best prior inventory).

kilotons per year	N. America	N. Europe	N. Siberia	Nenets-Komi	Khanty-Mansiysk
2013					
ACCMIPv5 (prior)	116	241	127	0.6	1.8
EDGAR_HTAPv2.2 (prior)	117	163	108	0.3	0.6
MACCity (prior)	117	244	129	0.6	1.9
ECLIPSEv5 (prior)	148	352	187	26	25
Posterior (ECLIPSEv5)	149±45	152±46	230±66	17±5	32±8
2014					
ACCMIPv5 (prior)	130	253	178	0.5	1.9
EDGAR_HTAPv2.2 (prior)	131	175	159	0.3	0.7
MACCity (prior)	131	256	179	0.5	1.8
ECLIPSEv5 (prior)	162	364	238	25	26
Posterior (ECLIPSEv5)	193±61	124±44	291±73	15±5	28±8
2015					
ACCMIPv5 (prior)	149	250	155	0.5	1.8
EDGAR_HTAPv2.2 (prior)	150	172	136	0.3	0.6
MACCity (prior)	150	252	156	0.6	1.8
ECLIPSEv5 (prior)	182	381	222	25	25
Posterior (ECLIPSEv5)	181±55	238±66	130±52	14±5	37±8
3-year average emissions	**174±58**	**170±59**	**217±69**	**15±5**	**32±8**

910   **FIGURES & LEGENDS**

911
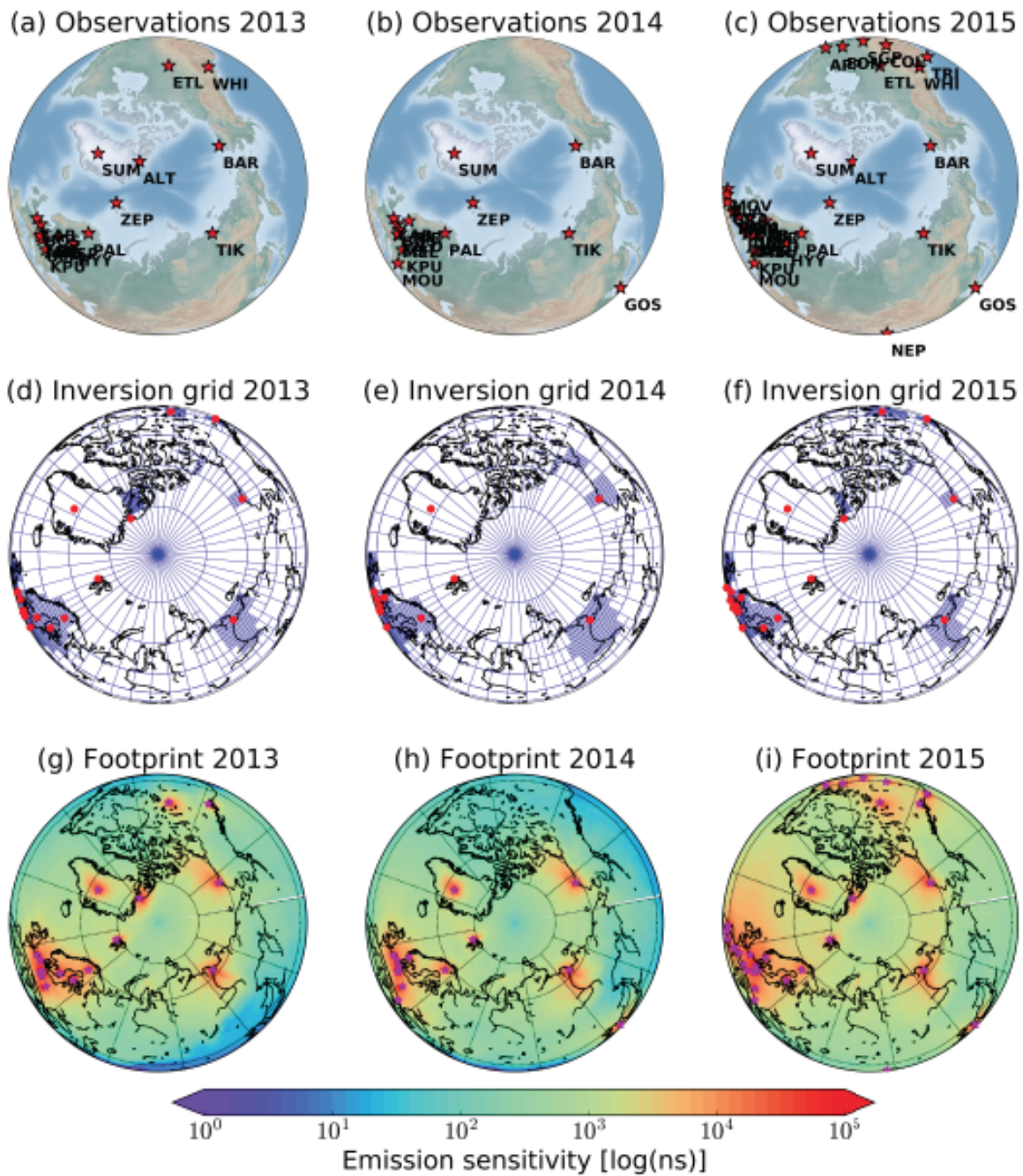
Figure 1. Observation network used for the present inversion (a, b and c), and variable-resolution grid used for the inversion (d, e, and f) also showing the location of the observation sites (red stars) for 2013–2015 period. Sensitivity to the surface emissions (i.e., the footprint emission sensitivity or equivalently source-receptor relationship) integrated over all observation sites and all time steps (g, h and i) for the years 2013, 2014 and 2015 (units of log(ns)).
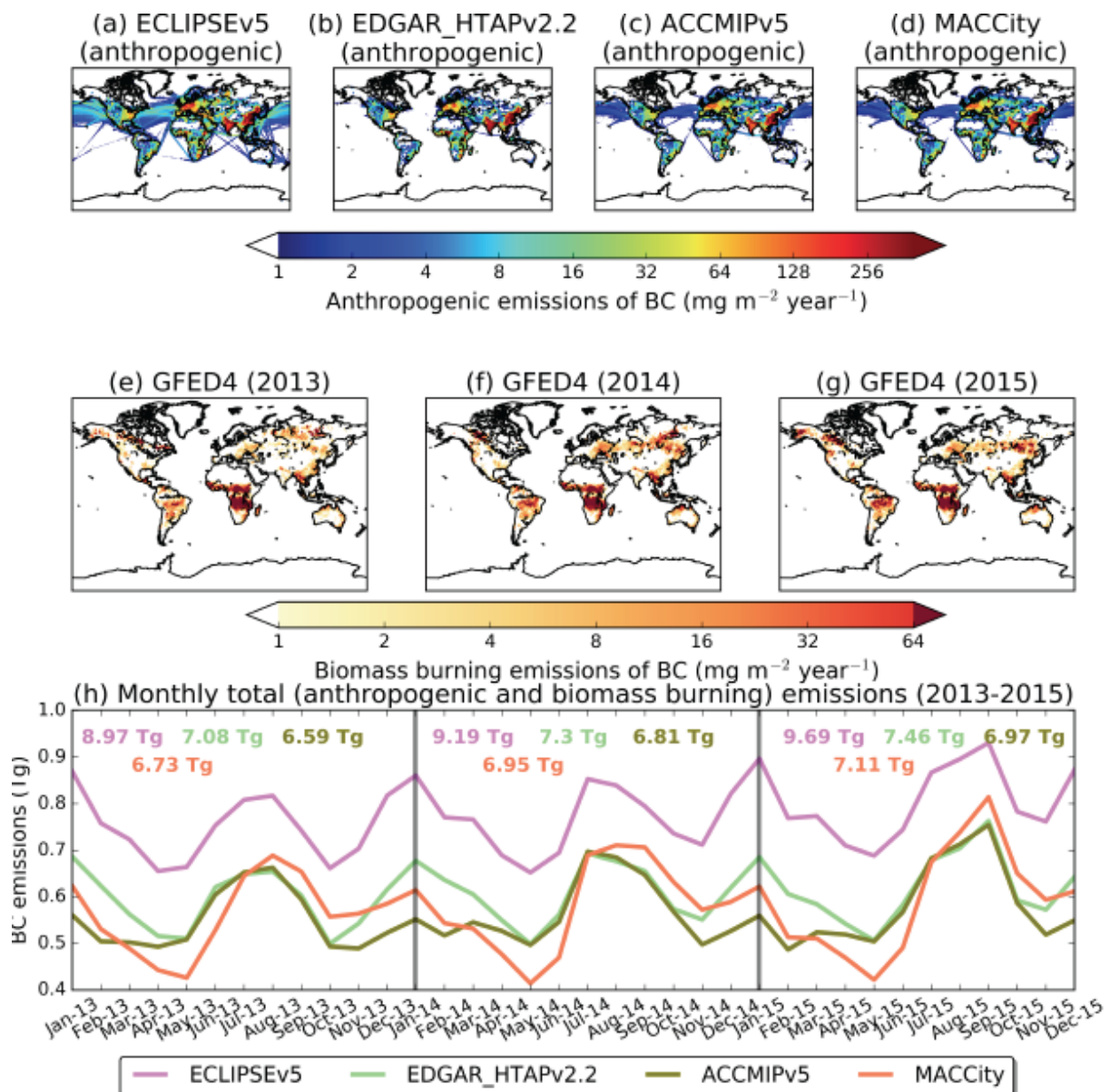
Figure 2. (a–d) Anthropogenic emissions of BC in the inversion domain (>50°N) from ECLIPSEv5, EDGAR_HTAPv2.2, ACCMIPv5 and MACCity (anthropogenic emissions are assumed to be constant throughout every year). (e–g) Biomass burning emissions from GFED4 for 2013, 2014 and 2015 (Giglio et al., 2013). (h) Monthly total (anthropogenic and biomass burning) BC emissions north of 50°N from 2013 to 2015 from the four prior inventories used for the inversion. Coloured numbers correspond to total annual BC from each emission inventory.
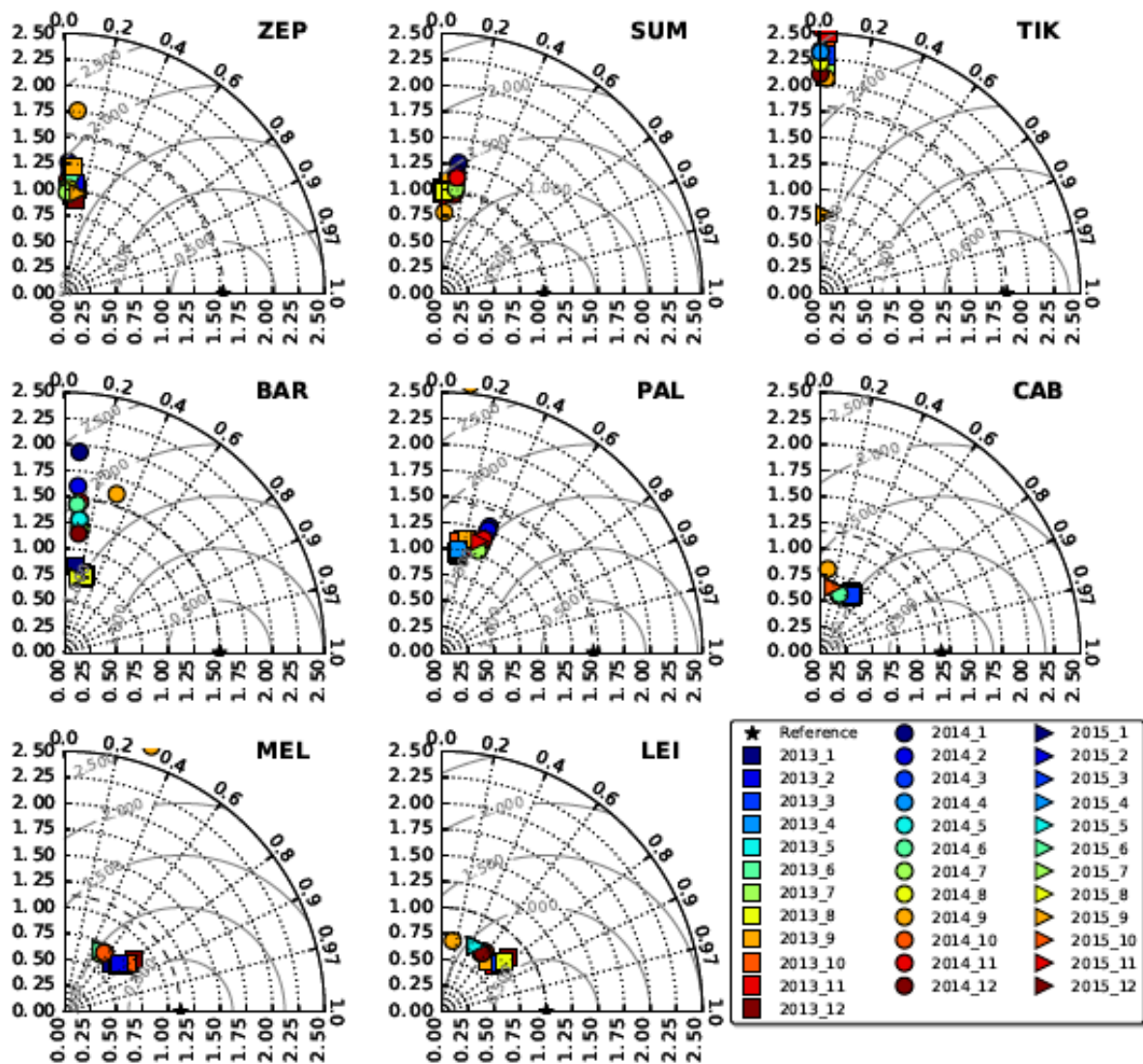
Figure 3. Taylor diagrams for the comparison of the prior (ECLIPSEv5) simulated concentrations with observations for all years (2013 – 2015) for 12 BC species with different scavenging coefficients (**Table 2**). The radius indicates standard deviations normalised against the mean concentration (NSD); the azimuthal angle the Pearson correlation coefficient, while the normalised (against observation) root mean square error (nRMSE) in the simulated concentrations is proportional to the distance from the point on the x-axis identified as "reference" (grey contours).

937

MONTHLY AVERAGE NMSE VALUES OF SIMULATED CONCENTRATIONS
AND OBSERVATIONS OF 12 BC SPECIES (2013-2015)

938
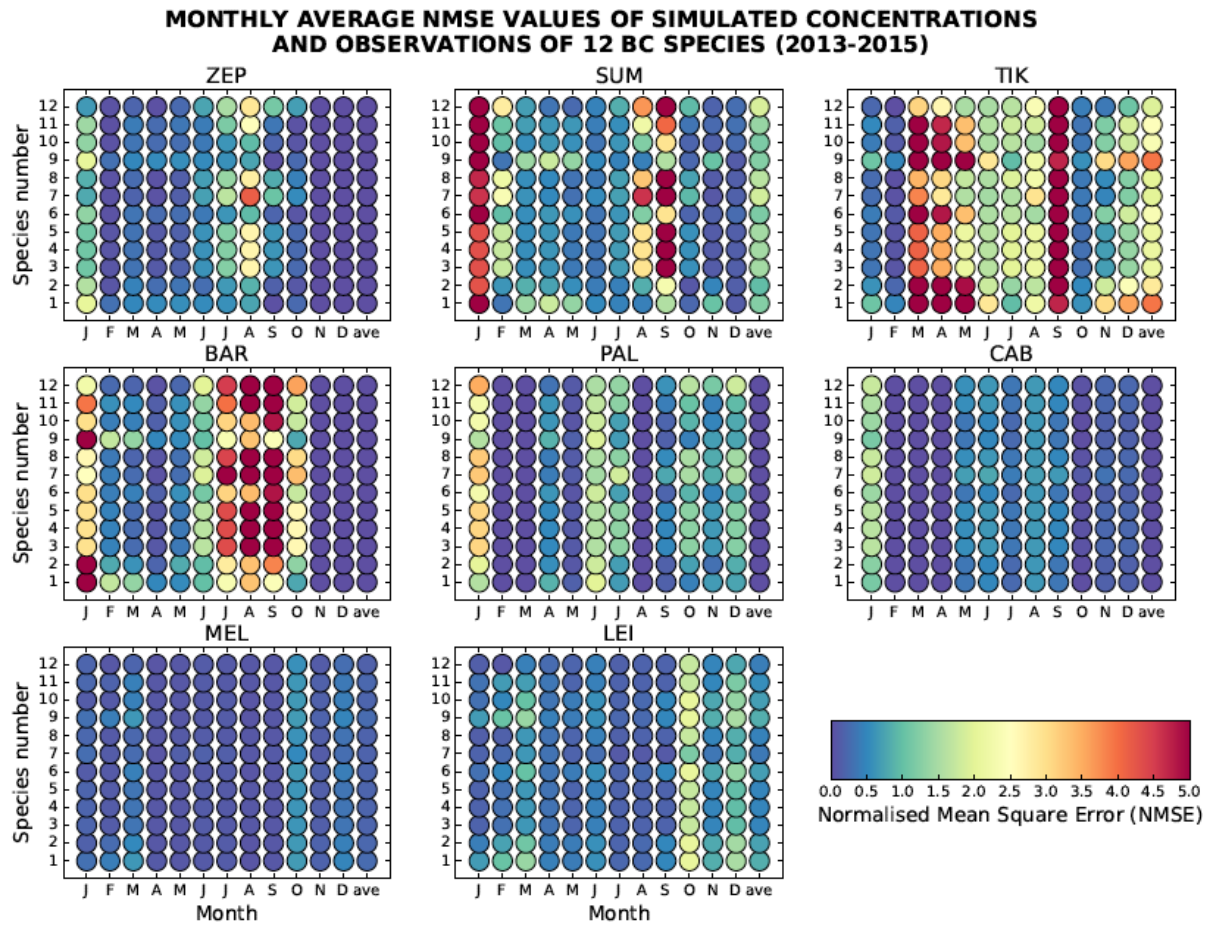
Figure 4. Monthly average NMSE values due to use of 12 different BC species defined in **Table 2** for the eight stations with complete data in the period 2013–2015. The annual mean is denoted as "ave").

942
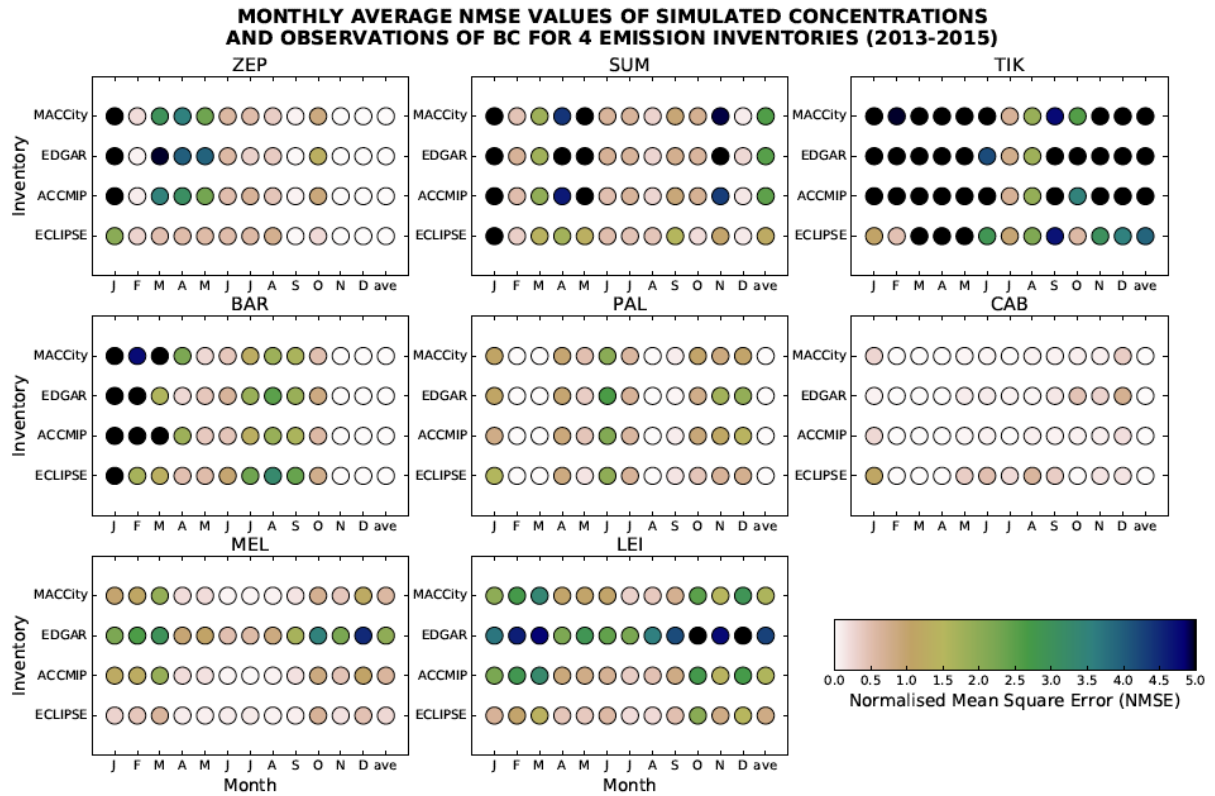
943

944   **Figure 5.** Monthly average NMSE values due to use of different emission inventories

945   (ECLIPSEv5, ACCMIPv5, EDGAR_HTAPv2.2, MACCity) for the eight stations with

946   complete data in the period 2013–2015. The annual mean is denoted as "ave").

947
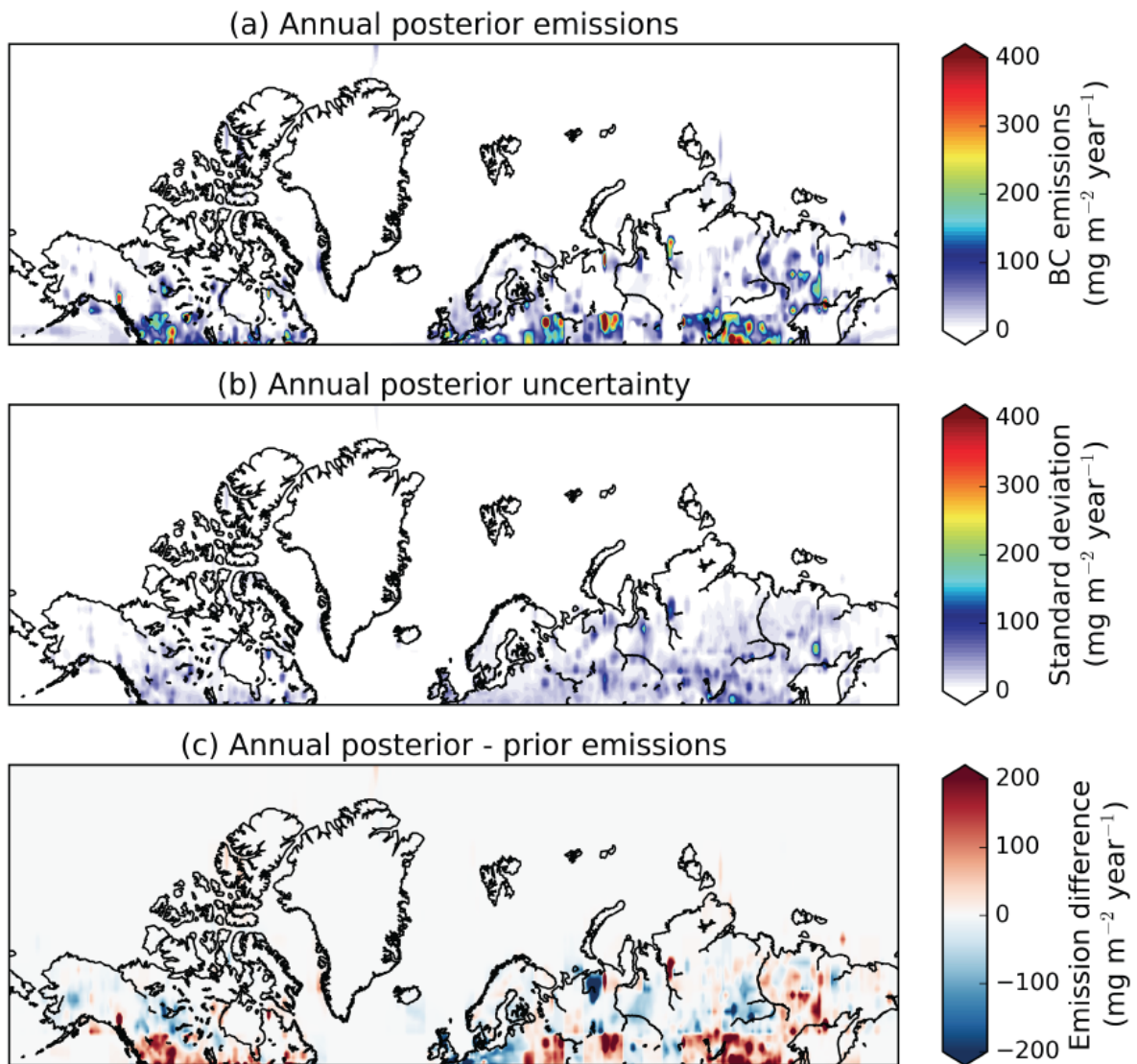
948
949 **Figure 6.** (a) Annual posterior emissions of BC in areas >50°N averaged for the period 2013–
950 2015, (b) average posterior uncertainty due to scavenging and use of different prior emissions
951 for the same period. (c) Difference between posterior and prior emissions for 2013–2015.

952

953

Figure 7. Comparison of prior (ECLIPSEv5, ACCMIPv5, EDGAR HTAPv2.2 and MACCity) and posterior simulated concentrations of BC with observations from the ACCACIA flight campaign near Zeppelin station, Ny-Ålesund in 2013 adopted from Sinha et al. (2017). The variability of the prior concentrations (shaded area) was calculated as the standard deviation of BC concentrations from the 12 species with different scavenging coefficients as shown in **Table 2**. Uncertainties of the posterior concentrations are due to scavenging and use of 4 different a priori datasets (section 3.4). RMSE values are computed for ECLIPSEv5 concentrations, all prior concentrations (average) and posterior simulated BC concentrations.

963

964
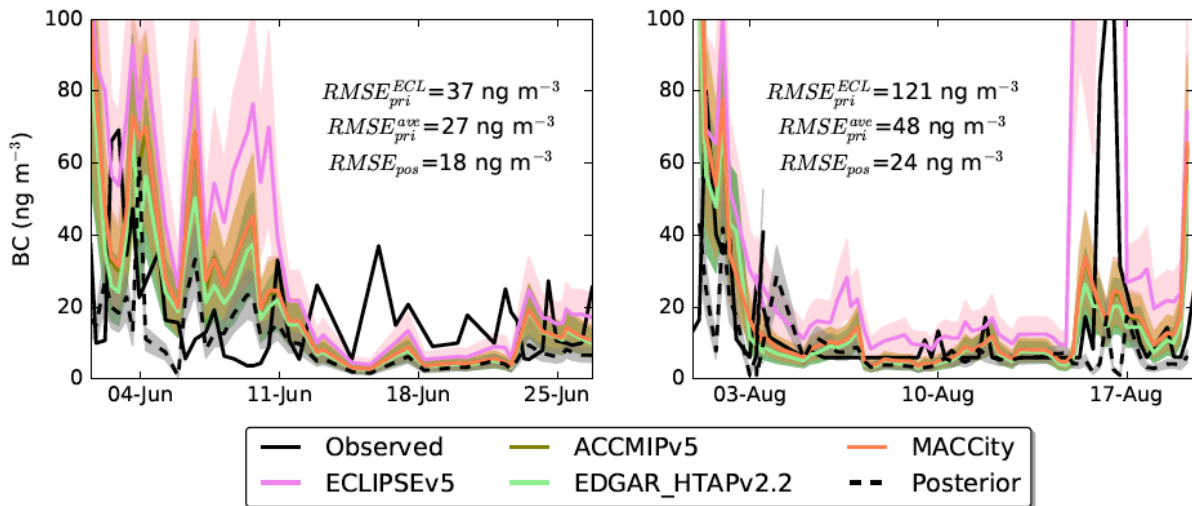
Figure 8. Comparison of prior (ECLIPSEv5, ACCMIPv5, EDGAR HTAPv2.2 and MACCity) and posterior simulated concentrations of BC with observations from a ship campaign in North Atlantic and Baltic Seas in 2014 adopted from Shevchenko et al. (2016). The variability of the prior concentrations (shaded area) was calculated as the standard deviation of BC concentrations from the 12 species with different scavenging coefficients as shown in **Table 2**. Uncertainties of the posterior concentrations are due to scavenging and use of 4 different a priori datasets (section 3.4). RMSE values are computed for ECLIPSEv5 concentrations, all prior concentrations (average) and posterior simulated BC concentrations.

973
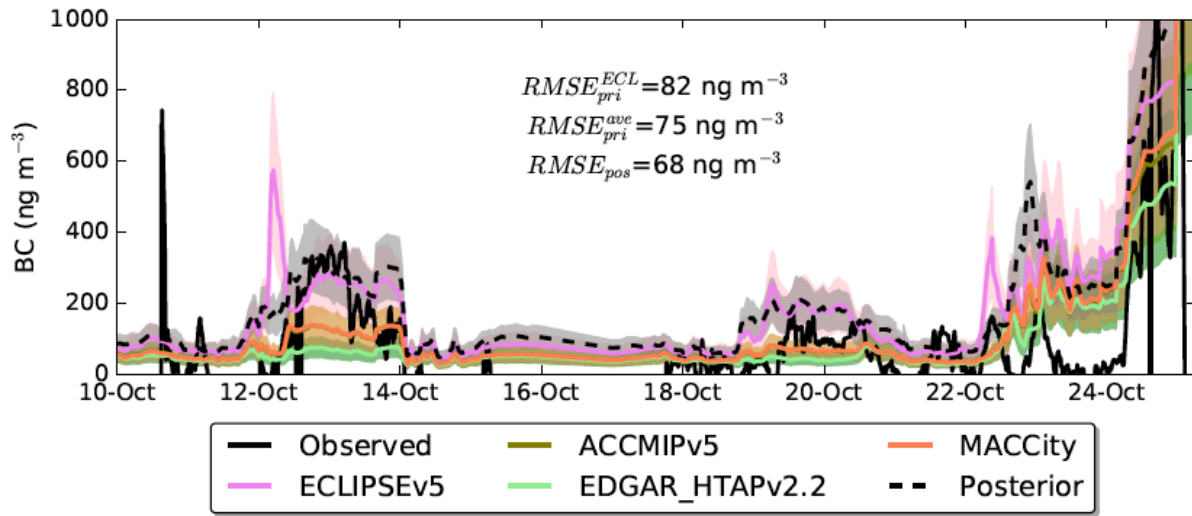
Figure 9. Comparison of prior (ECLIPSEv5, ACCMIPv5, EDGAR HTAPv2.2 and MACCity) and posterior simulated concentrations of BC (2015) with observations from a ship campaign in the Russian Arctic in 2015 adopted from Popovicheva et al. (2017). The variability of the prior concentrations (shaded area) was calculated as the standard deviation of BC concentrations from the 12 species with different scavenging coefficients as shown in **Table 2**. Uncertainties of the posterior concentrations are due to scavenging and use of 4 different a priori datasets (section 3.4). RMSE values are computed for ECLIPSEv5 concentrations, all prior concentrations (average) and posterior simulated BC concentrations.
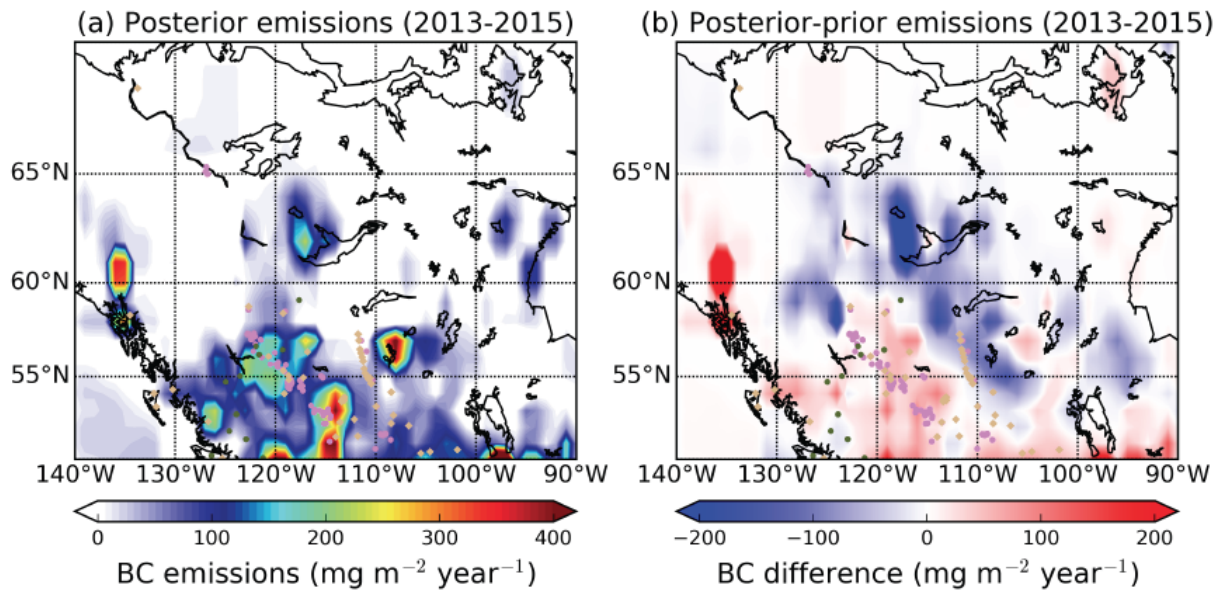
984

985 **Figure 10.** (a) Optimised emissions of BC in North America (Western Canada) averaged over
986 the 2013–2015 period. (b) Difference between a posteriori and a priori emissions of BC
987 (ECLIPSEv5 was used as the prior). Magenta points on the map denote the gas flaring
988 industries from the Global Gas Flaring Reduction Partnership (GGFR)
989 (http://www.worldbank.org/en/programs/gasflaringreduction), grey points show the power
990 industries that operate using fossil fuels and oil and gas production and oil refining industries
991 adopted from Industry About (https://www.industryabout.com/canada-industrial-map), while
992 dark green points show active fires from MODIS.

993
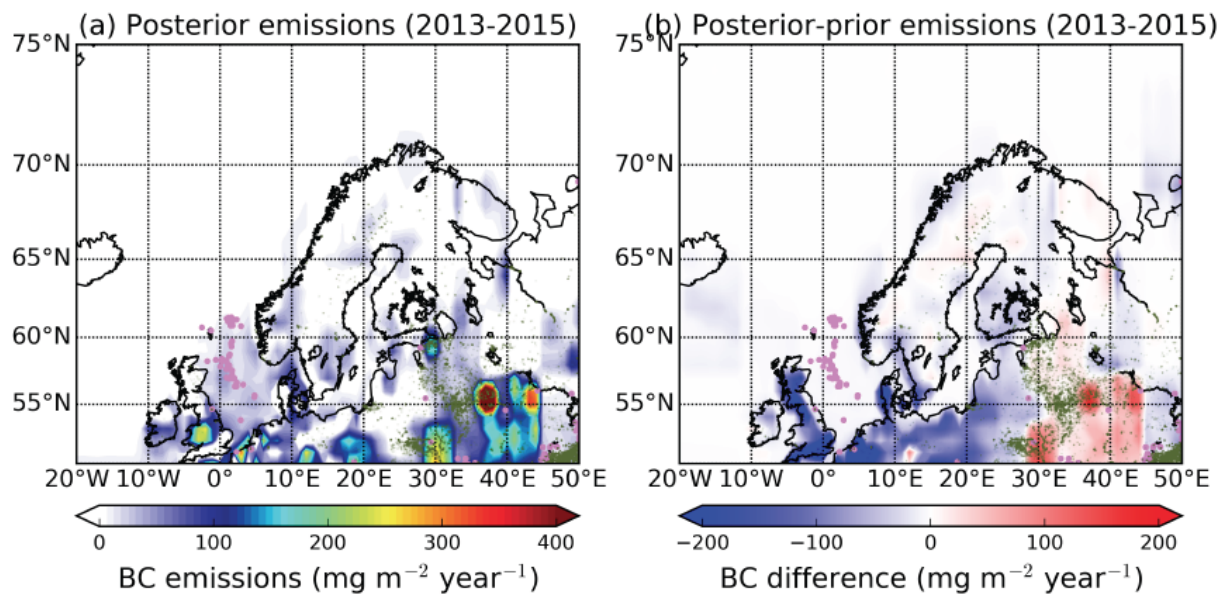
994

995   **Figure 11.** (a) Optimised emissions of BC in Northern Europe averaged over the 2013–2015

996   period. (b) Difference between a posteriori and a priori emissions of BC (ECLIPSEv5 was

997   used as the prior). Magenta points on the map indicate the gas flaring industries from the

998   Global   Gas   Flaring   Reduction   Partnership   (GGFR)

999   (http://www.worldbank.org/en/programs/gasflaringreduction), while dark green points show

1000 the vegetation fires adopted from Hao et al. (2016).

1001
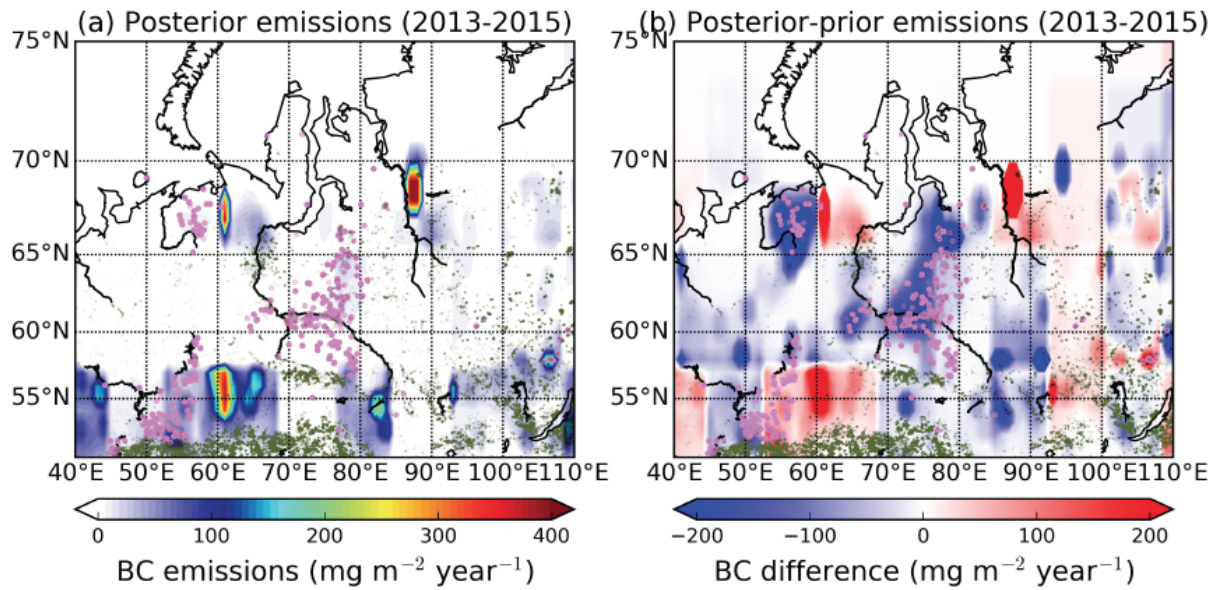
Figure 12. (a) Optimised emissions of BC in Western Siberia averaged for the 2013–2015 period. (b) Difference between a posteriori and a priori emissions of BC (ECLIPSEv5 was used as the prior). Magenta points on the map indicate the gas flaring industries from the Global Gas Flaring Reduction Partnership (GGFR) (http://www.worldbank.org/en/programs/gasflaringreduction), while dark green points show the vegetation fires adopted from Hao et al. (2016).
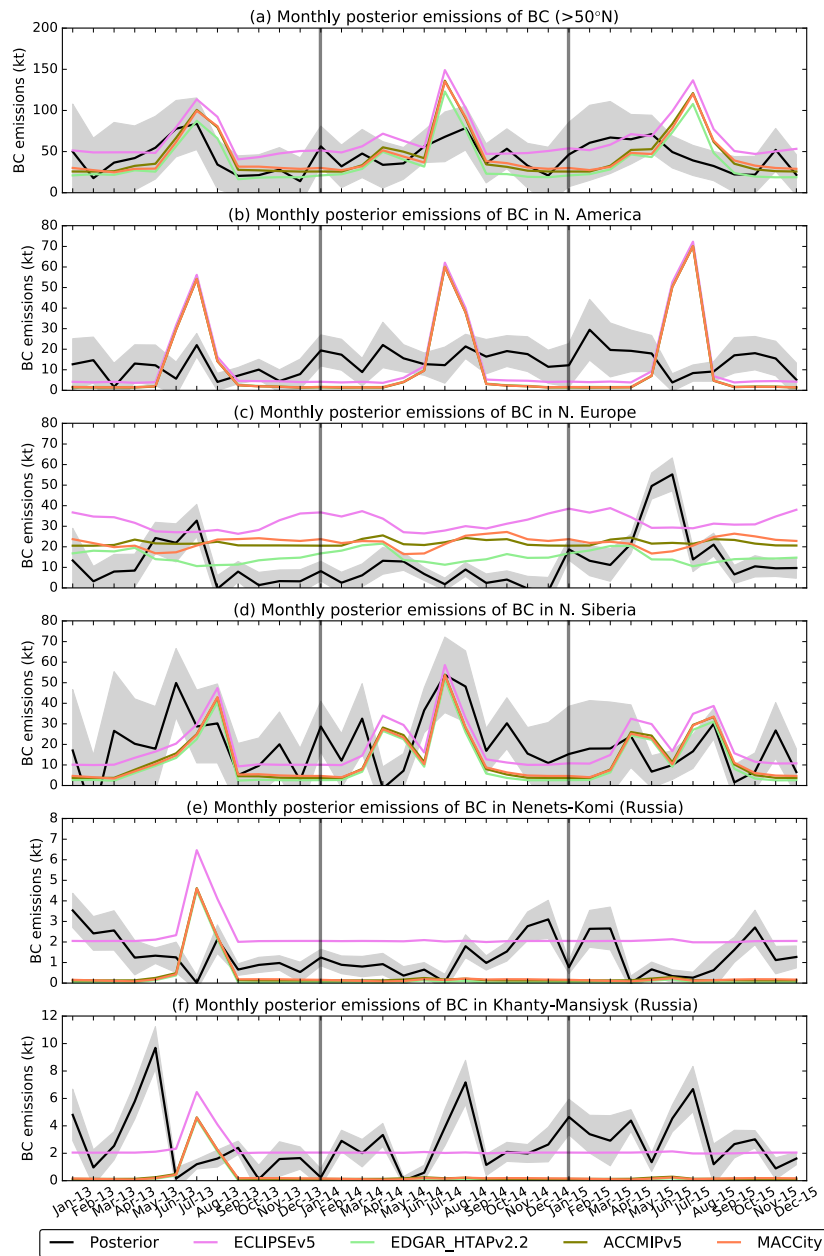
Figure 13. Monthly posterior emissions of BC shown for all regions located (a) >50°N, (b) in North America (>50°N), (c) North Europe (>50°N), (d) North Siberia (>50°N), (e) Nenets-Komi oblast (>50°N, Russia) and (f) Khanty-Mansiysk oblast (>50°N, Russia) for the 2013–2015 period. Monthly prior emissions of BC from ECLIPSEv5, EDGAR_HTAPv2.2, ACCMIPv5 and MACCity emissions inventories are also shown for the same regions and time period. The uncertainty of the posterior emissions of BC stems from the use of different scavenging coefficients and different prior emission datasets (see section 3.3).

 SUPPLEMENTARY FIGURES & LEGENDS

1019

1020   **Figure S 1.** Taylor diagrams for the comparison of the prior simulated concentrations with

1021   observations for all years (2013 – 2015) for 12 BC species with different scavenging

1022   coefficients (**Table 2**). The radius indicates standard deviations normalised against the mean

1023   concentration (NSD); the azimuthal angle the Pearson correlation coefficient, while the

1024   normalised (against observation) root mean square error (nRMSE) in the simulated

1025   concentrations is proportional to the distance from the point on the x-axis identified as

1026   "reference" (grey contours). The results refer to the use of ACCMIPv5, EDGAR_HTAPv2.2

1027   and MACCity as the prior emissions.

1028

1029   **Figure   S   2.**   Monthly   average   relative   model-observation   mismatches

1030   ([$model - observations$]/$observations$) for prior simulated (average values from all

1031   four inventories used) concentrations of BC due to the perturbation of scavenging parameters

1032   according to **Table 2** for the inversions of 2013, 2014 and 2015.

1033

1034   **Figure S 3.** Monthly average model-observation mismatches ([$model - observations$]/

1035 $observations$) for prior simulated concentrations of BC (best species) due to use for four

1036   different   emission   inventories   (ECLIPSEv5,   ACCMIPv5,   EDGAR_HTAPv2.2   and

1037   MACCity) for the inversions of 2013, 2014 and 2015.

1038

1039   **Figure S 4.** Taylor diagrams for the comparison of the posterior simulated concentrations

1040   with observations for all years (2013 – 2015). The radius indicates standard deviations

1041   normalised against the mean concentration (NSD); the azimuthal angle the Pearson

1042   correlation coefficient, while the normalised (against observation) root mean square error

1043   (nRMSE) in the simulated concentrations is proportional to the distance from the point on the

1044   x-axis identified as "observed" (grey contours).

1045

1046   **Figure S 5.** (a, c, e) Optimised emissions of BC in North America (Western Canada) for

1047   2013, 2014 and 2015. (b, d, f) Difference between a posteriori and a priori emissions of BC

1048   (ECLIPSEv5 was used as the prior). Magenta points on the map denote the gas flaring

1049   industries   from   the   Global   Gas   Flaring   Reduction   Partnership   (GGFR)

1050 (http://www.worldbank.org/en/programs/gasflaringreduction), grey points show the power

1051 industries that operate using fossil fuels and oil and gas production and oil refining industries

1052 adopted from Industry About (https://www.industryabout.com/canada-industrial-map), while

1053 dark green points show active fires from MODIS.

1054

1055 **Figure S 6.** (a, c, e) Optimised emissions of BC in Northern Europe for 2013, 2014 and 2015.

1056 (b, d, f) Difference between a posteriori and a priori emissions of BC (ECLIPSEv5 was used

1057 as the prior). Magenta points on the map indicate the gas flaring industries from the Global

1058 Gas Flaring Reduction Partnership (GGFR)

1059 (http://www.worldbank.org/en/programs/gasflaringreduction), while dark green points show

1060 vegetation fires adopted from Hao et al. (2016).

1061
1062 **Figure S 7.** (a, c, e) Optimised emissions of BC in Western Siberia for 2013, 2014 and 2015.

1063 (b, d, f) Difference between a posteriori and a priori emissions of BC (ECLIPSEv5 was used

1064 as the prior). Magenta points on the map indicate the gas flaring industries from the Global

1065 Gas Flaring Reduction Partnership (GGFR)

1066 (http://www.worldbank.org/en/programs/gasflaringreduction), while dark green points show

1067 forest fires adopted from Hao et al. (2016).